NTNU – Trondheim
Norwegian University of
Science and Technology

Oxygen evolution on $La_{1-x}Sr_xCoO_3$ Pellet-Electrodes in alkaline Solution

Charge Carrier density dependence of
electrocatalytic activity

Erik Bjartnes

Materials Science and Engineering
Submission date: June 2012
Supervisor: Svein Sunde, IMTE

Norwegian University of Science and Technology
Department of Materials Science and Engineering

Abstract

Alkaline water electrolysis need a catalyst with low overpotential and high current densitiy for oxygen evolution in order to be a commercial viable hydrogen source in the future. Finding and establishing a correlation between electrocatalytic activity and charge carrier density will help towards finding an optimum catalyst for this purpose. Such comparisons have been made using theoretical values for charge carrier density, but the aim of this work is to use charge carrier data from experimental values.

Five powders of $La_{1-x}Sr_xCoO_3$ (with compositions x = 0, 0.25, 0.5, 0.75, 1) were synthesized by solid-state synthesis and sintered to pellets. The pellet surfaces were investigated in alkaline solution (pH = 13) by cyclic voltammetry, polarization and impedance measurements. Polarization curves with Tafel lines and Mott-Schottky plots were established. The powders and pellet surfaces were investigated by XRD, SEM, EDS, AFM and light microscope.

The polarization curves revealed a volcanic behavior with an increase in catalytic activity from x = 0 up to x = 0.75 and then decreasing. The charge carrier density increased with increasing strontium doping. The resulting comparison gave figure 34. Surface investigation revealed much porosity. Because of corrosion, the surface area increased with measuring, and finding the real surface area and the roughness proved to be problematic.

A volcanic behavior of the charge carrier density and electrocatalytic activity relationship were observed. Finding roughness factor values by measuring double layer capacitance measured by the cyclic voltammetry method and dividing by the nominal capacitance for a flat surface proved to be unsuccessful. Better synthesis and sintering procedures of pellets are needed to increase the density of the samples in order to decrease the roughness and the effect of corrosion.

Contents

1 Introduction

Today, energy origins mainly from fossil fuels. As this resources are limited and the world energy demand rises, new energy sources and energy carriers must be adopted. An energy carrier must be a medium where energy can be stored, transported and utilized again with minimal loss. Such potential energy carriers can be the battery or hydrogen.

The principle for use of hydrogen as an energy carrier is very simple. Electrical energy from green energy sources is converted to hydrogen by water electrolysis, stored, transported and clean electrical energy is recovered in a fuel cell. Minimizing the loss of energy for each of these conversion steps is very important.

Alkaline water electrolysis is the classical technique for hydrogen production. One of the main challenges of todays electrolysis is achieving a higher current density than the typical values of 1-2 kA/m^2. This prospect requires a stable electro-catalyst with high current density and low overpotential.

The perovskite oxides $La_{1-x}Sr_xCoO_3$ is a mixed conductor (ionic and electronic conductor). These oxides receive a lot of attention today due to their many potential uses. This can be as electrode material for SOFC (Solid Oxide Fuel Cells), gas separation membranes, sensors, high temperature-superconductors or, as studied in this case, oxidation catalyst.

The goal of this work is to study the correlation between oxygen evolution properties and the charge carrier density at the surface. This comparison has been been studied by using theoretical values for the charge carrier densities by e.g. *Suntivich* et. al [13]. The focus of this work is to, instead of theoretical data, use experimental charge carrier density data from the pellet surface.

For this purpose, 5 pellet samples of $La_{1-x}Sr_xCoO_3$ with different x values (0, 0.25, 0.5, 0.75, 1) have been synthesized, sintered and electrochemically measured in alkaline solution.

2 Theory

2.1 The Oxygen Reaction

In alcaline water electrolysis, water reacts and form oxygen and hydrogen by the reaction:

$$4OH^-_{(aq)} \rightleftharpoons 4OH_{(ads)} + 4e^- \rightleftharpoons 2H_2O_{(l)} + O_{2(g)} + 4e^- \quad (1)$$

$$2H_2O_{(l)} + 2e^- \rightleftharpoons H_{2(g)} + 2OH^-_{(aq)} \quad (2)$$

This process can't occur faster than the slowest reaction. Oxygen is formed at the cathode by adsorbing hydroxyl groups and this is the rate-determining reaction. It is also this reaction which requires the most overpotential as it is more complex. First, four OH^- molecules are absorbed at the surface and form a relative weak oxygen-oxygen bond [7]. Four electrons are adsorbed and it is then desorbed with as oxygen and water. This is a simple evaluation of the oxygen reaction. Many smaller reaction steps have been presented by other authors, but are not presented here.

2.2 Band Theory

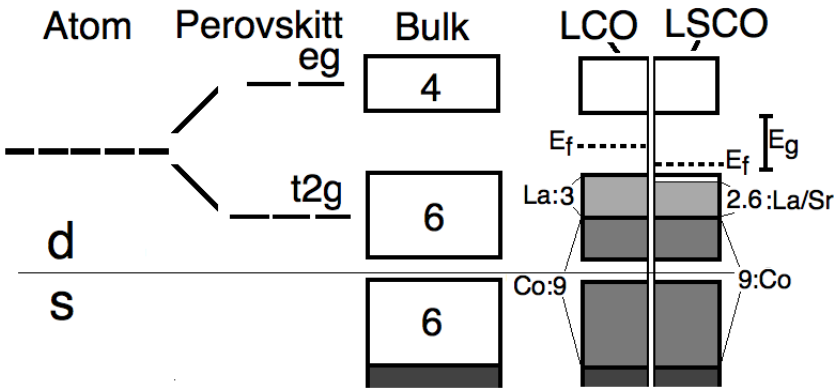

Figure 1: Band splitting and band filling in a perovskite with the examples of $LaCoO_3$ and $La_{0.6}Sr_{0.4}CoO_3$. E_G = Energy gap. E_F = Fermi energy. [1]

$La_{1-x}Sr_xCoO_3$ is a perovskite where oxygen atoms forms the octahedra and cations are placed in the octahedra positions. Two of the five d-orbitals in the cation is oriented towards the oxygen atoms and the filling of these orbitals requires more energy. The d-orbitals are therefore split into two bands: the high energy band e_g and the low energy band t_{2g}, rooming 4 and 6 electrons respectively. In $LaCoO_3$ will the oxygen atoms allow for up to 6 atoms in the s-band. Cobolt is $3d^74s^2$ with a total of 9 valence electrons and lanthanum is $5p^16s^2$ with a total of 3. This results in the t_{2g} being completely filled and the e_g band being empty and the material is an intrinsic semiconductor. When doping with strontium, which is $5s^2$ and has only 2 valence electrons, the amount of electrons in the t_{2g} is reduced to $0,6 \cdot 3 + 0,4 \cdot 2 = 2,6$ electrons as shown in figure 1. The resulting material is a p-doped extrinsic semiconductor with acceptors being the majority charge carrier.

Previous work revealed that $La_{1-x}Sr_xCoO_3$ is experiencing a depletion of oxygen atoms from the surface at low potentials. This depletion is marked with δ and the resulting formula is then $La_{1-x}Sr_xCoO_{3-\delta}$. The depletion of oxygen atoms will n-dope the material because the oxygen leaves electrons behind. *Bezdicka* et. al. [9] reported δ values as large as 0.5. At low potentials, the oxygen vacancies will therefore dope the material significantly.

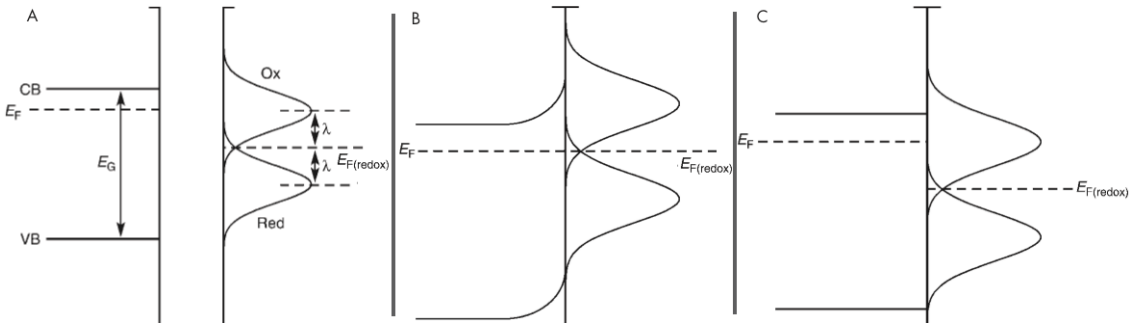

Figure 2: A: Energy levels for a n-doped semiconductor and an electrolyte. CB and VB: conduction band and valence band. Ox and Red: Redox states which correspond to the Fermi-level in the solution: $E_{F(redox)}$. B: Electronic equilibrium at contact. In the semiconductor a depletion layer occur and cause band bending. C: The potential is changed to the semiconductors flat-band potential. [4]

2.3 Semiconductor electrolyte interface

At a semiconductor-electrolyte interface will the majority charge carriers, given a doped semiconductor, pass the interface and cause a band bending, as shown in figure 2 B. If a potential is adjusted, by using a potentiostat, to a state where the bands are no longer bending, the potential is equal to the semiconductors flat-band potential, V_{fb}.

In the ideal oxygen catalyst, the conduction band and the valence band must enclose the energy levels for oxygen and hydrogen evolution and in addition their overpotentials. Figure 3 shows the energy gap for a such an perfect catalyst to the right. Large band gaps usually results in large overpotentials (ZnO), while a too short band gap may prevent the reaction from occurring (GaAs). Finding V_{fb} will help to locate the valence band as the potential difference between them is small.

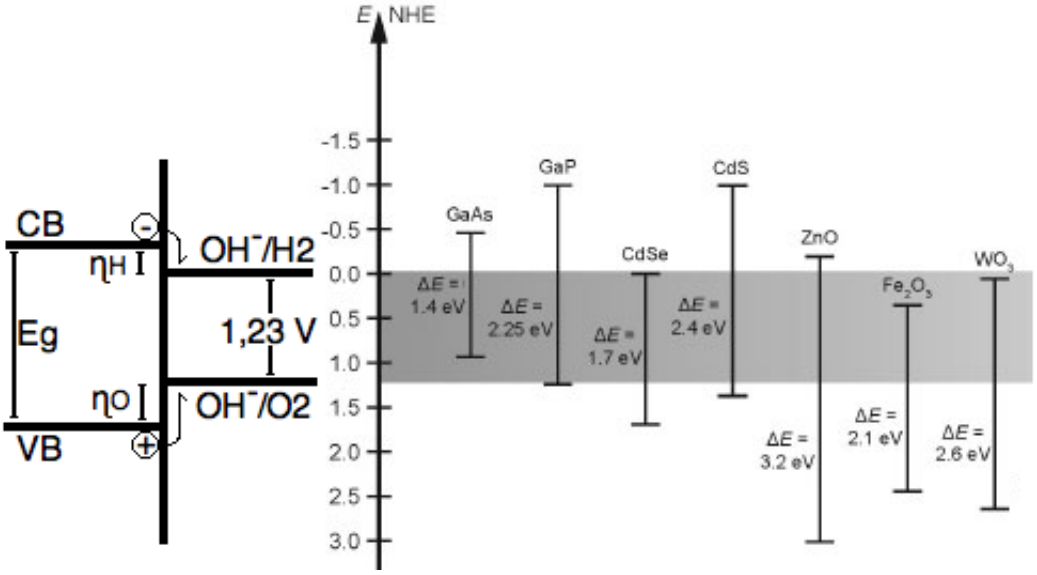

Figure 3: Relationship between the energy levels in the semiconductor and the oxygen reaction. η is the overpotential. Band gaps for some known materials are given to the left.

2.4 Impedance

The flat band potential may be located by impedance measurement. Impedance is a frequency dependent resistance found by applying AC voltage to the system. How fast the system responds is then measured by measuring the real and the imaginary resistance. The system can be interpreted as the circuit shown in figure 4

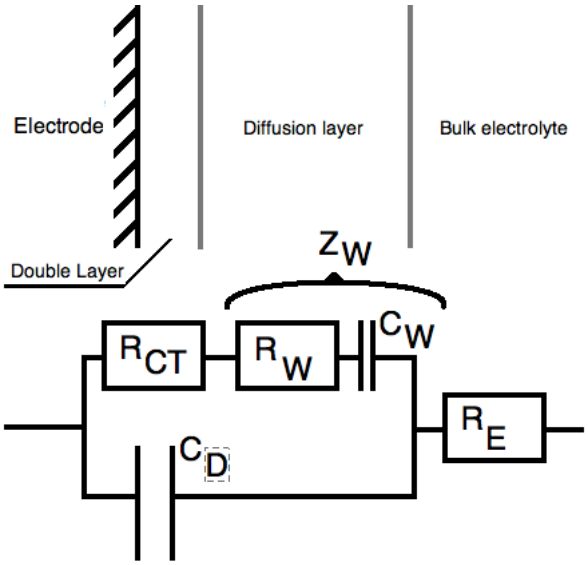

Figure 4: Equivalent electric curcuit for a half-cell. R_{CT} is the electron transfer resistance. R_W and C_W is the double layers resistance and capacitance which is the Warburg-impedance: Z_W. R_E is resistance in the electrolyte and C_D is the double layer capacitance. [1].

The resulting resistances is explained by the following equation:

$$Z = R_E + \frac{R_{CT} - i\omega R_{CT}^2 C_D}{1 + \omega^2 R_{CT}^2 C_D^2} \tag{3}$$

The resistance can also be expressed as Z = Re(Z) + Im(Z) where the imaginary part can be written as:

$$|Im(Z)| = \frac{\omega R_{CT}^2 C_D}{1 + \omega^2 R_{CT}^2 C_D^2} \tag{4}$$

If R_{CT}, C_D and R_E in equation (3) are constant, and ω is a variable, it will form a semi-circle in the complex plane:

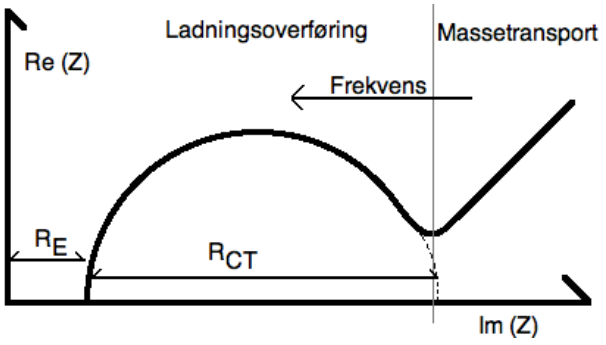

Figure 5: Theoretical Nyquist plot for the circuit in figure 4. [1]

At low frequencies, the system is regulated by charge transfer. If the frequency is high enough, the reaction is no longer determined by the slow diffusion processes, but regulated by charge transfer. If the frequency is high, $\omega^2 R_{CT}^2 C_D^2 >> 1$, and equation(4) can be simplified to:

$$|Im(Z)| = \frac{1}{\omega C_D} \tag{5}$$

This equation can be used to find the capacitance at high frequency. This capacitance can in return be used to find the flat band potential which are related by the Mott-Schottky equation [4]:

$$\frac{1}{C_D^2} = (\frac{2}{\epsilon\epsilon_0 A^2 e N_D})(V - V_{FB} - \frac{k_b T}{e}) \tag{6}$$

where e is the electron charge, N_D is the charge carrier density ϵ is the dielectric permittivity of the semiconductor, ϵ_0 is the permittivity of vacuum, T is the temperature, k_b is the Boltzmann constant and A is the electrode surface area. By plotting $\frac{1}{C_D^2}$ versus potential wil result in a linear curve which intersects the x-axis in $V_{FB} + (\frac{k_b T}{e})$ where $(\frac{k_b T}{e})$ is about 25mV at room temperature. Charge carrier density can be found from the slope of this curve:

$$\frac{d(\frac{1}{C_D^2})}{dV} = (\frac{2}{\epsilon\epsilon_0 A^2 e N_D}) \tag{7}$$

2.5 The Tafel equation

The relationship between current densities and overpotentials can usually be described by Tafel equations. These equations describe the linear parts of the curve in a E - log i diagram as illustrated in figure 6. The Tafel equation is:

$$\eta = b \cdot log(\frac{i}{i_0}) \tag{8}$$

Where η is the overpotential, b is the Tafel slope, i is the current density and i_0 is the exchange current density. i_0 is the current density at zero overpotential. In this case this is the current at the reversible potential for oxygen evolution at 1.23 V. The Tafel slope describes how the current density increase with increasing overpotential.

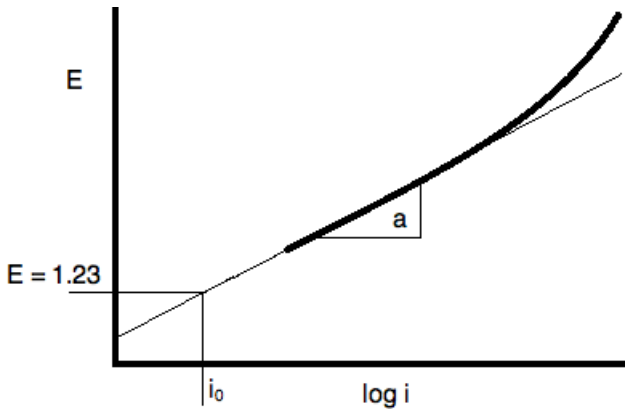

Figure 6: Figure illustrating a typical polarization curve and the linear Tafel line.

3 Experimental

3.1 Synthesis of powders

Table 1: The chemicals used in this work

Compound	Company	Purity
La_2O_3	Sigma-Aldrich Norway AS	$\geq$ 99.99%
$SrCO_3$	Merck KGaA	$\geq$ 98.5%
Co_3O_4	Sigma-Aldrich Norway AS	-
$NaOH$	Merck KGaA	$\geq$ 99.98%
$etOH$	VWR International AS	$\geq$ 99.8%

The powders were synthesized by a solid-state synthesis method. La_2O_3 and $SrCO_3$ are first dried in separate Al_2O_3 crucibles at 700 °C for four hours. This is because La_2O_3 has a high affinity to water and hydroxyl groups must be removed. It is unsure if this is necessary for $SrCO_3$. The powders must be employed shortly after drying to avoid moisturisation. The correct amount of La_2O_3, $SrCO_3$ and Co_3O_4 is calculated based on the final composition. The compositions for the five samples are given in table 2. The powders are solved in absolute ethanol and milled in a planetary ball mill for 15 minutes with 300 rpm. The container and the five milling balls are made of ZrO and have diameters of 250 mm and 30 mm respectively. Afterwards the ethanol is evaporated gently off in a rotary evaporator. The powder is transferred to an Al_2O_3 crucible and calcinated at 1000 °C for 12 hours. All heating rates in this work are at 200 °C/h. X-Ray Diffraction (XRD) were measured for each powder.

Table 2: The amount of each chemical for the different compositions for 20 g final product of $La_{(1-x)}Sr_xCoO_3$.

Amount	x=0	x=0.25	x=0.5	x=0.75	x=1
La_2O_3 [g]	13.25	10.43	7.40	3.93	0
$SrCO_3$ [g]	0	3.17	6.70	10.68	15.18
Co_3O_4 [g]	6,53	6.89	7,29	7.74	8.25

3.2 Sintering and preparation of pellets

The calcinated powder was weighted in samples of 1g, placed in a 10 mm diameter cylinder, and pressed with a mono axial press with 0.5 t load. This equals ∼60 MPa. The green bodies were then transferred to the oven and sintered at 1200 °C for 6 hours. After sintering the pellets shrank to a diameter of 9 mm and an area of 0.636 cm^2. All current densities in this work are divided by this area. After cooling, the pellets were embedded into epoxy and polished on both sides. See picture 9. The side which would face the electrolyte was polished. The final particle size of the polishing medium was 3 μm. The backside were only ground, not polished, and was relatively rough.

The pellets were mounted in a sample holder, which is a device used to ensure good electrical contact, isolation against the electrolyte, and the possibility to mount and unmount samples. See picture 9. Colloidal suspended silver were added between the pellets backside and the copper contact of the sample holder to ensure good contact. This is important in order to avoid the influence of a Schottky contact on the pellets backside.

3.3 Electrolyte and setup

The electrolyte solution were made by mixing 6 g of NaOH pellets into 150 ml H_20. Although this should give 1 M of OH^-, the pH were measured to about 13.0 $\pm$ 0.1. This is probably due to the degradation of the NaOH pellets. A hydrogen electrode made in the same electrolyte as the experiments was used as a reference. All potential values in this work is with respect to this reference. The counter electrode is a platinum electrode with 5 cm^2 surface area.

3.4 Electrochemical characterization

Electrochemical measurements of oxide pellets can be very challenging. As the surface is reduced and oxidized with on polarization, the results will vary with the settings. For example will an impedance measurement, measured with increasing or decreasing voltage give different results. This is probably due to the formation of oxygen vacancies as mentioned in section 2.2. Corrosion will also change the surface area, and this was one of the greater challenges in this work.

The electrochemical results presented in this work started with initial cyclic voltammetry (CV) in the potential area of 0.4 to 1.2 V with sweep rate 20 mV/s for one hour. This was done right after the surface had been ground and polished. These CV are intended to remove any impurities on the surface. After this, the electrodes were anodized at 1.4 V for 10 minutes in order to oxidize the surface and reach a steady state before polarization. This step prevents additional oxidation reactions from interfering with the oxygen evolution. The sweep rate for the polarization curves were 0.5 mV/s measured from 1 to 1.8 V and back down to 1.2 V. At this potential, additional CVs were measured with 10, 2, 5, 1 and 3 mV/s in a small voltage range (1.2-1.3 V). These CV were used to derive the double layer capacitance. The electrodes were then anodized again at 1.4 V for 10 minutes before the impedance measurements. The impedance measurements were recorded in a series from 1.4 to 0.4 V with steps of 0.05 V. The electrodes spent 1 minute at constant potential between each impedance measurement in order to stabilize. The frequency ranged from 10 kHz to 1 Hz with 2 measurements per decade. The amplitude was 10 mV. The first part of measurements are illustrated in figure 7.

Afterwards, additional measurements were taken in no particular order. More polarization curves were taken to investigate the current density and surface area increase and impedance measurements were taken to investigate reproducability, polarization effects, etc.

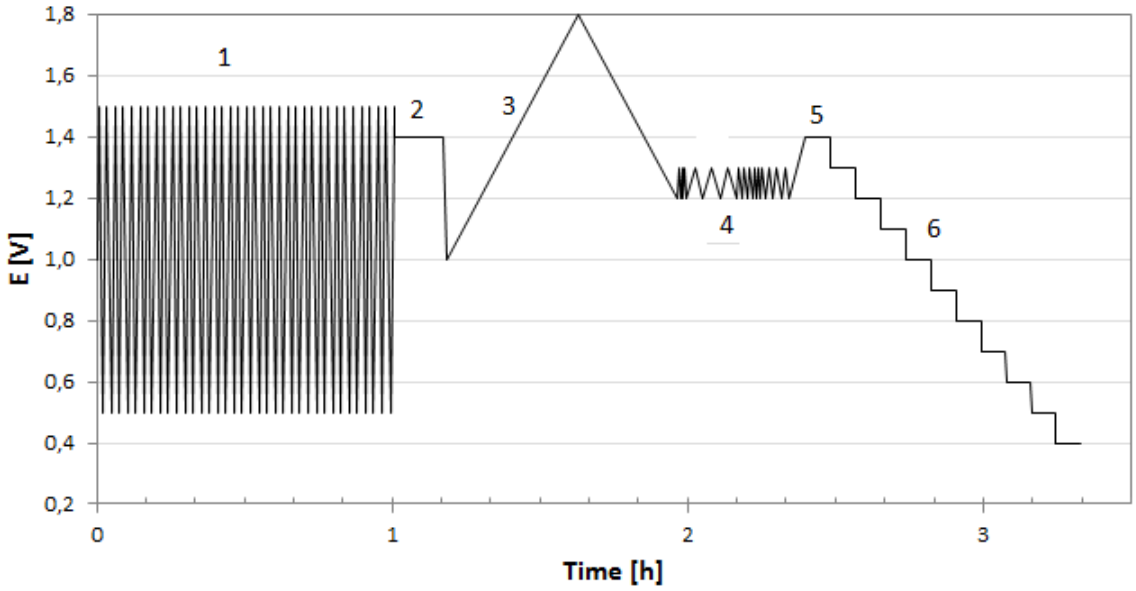

Figure 7: Graph shows a typical potential progression of the first round of electrochemical characterization. 1: CV with 20mv/s sweep rate. 2: Anodized at 1.4 V for 10 minutes. 3: Polarization measurement with 0.5 mV/s scan rate. 4: CV with different sweep rates for C_{DL} measurements. 5: Anodized at 1.4 V for 10 minutes. 6: Impedance series measurement from high to low potential.

3.5 Surface investigation

The porosity and the surface roughness of the pellets are a result of the synthesis, sintering and the electrochemical procedure. The change in roughness is directly interfering with the electrochemical results. Investigating and measuring the surface roughness of the pellets was therefore important. Light microscope, AFM (Atomic Force Microscope), SEM and EDS were used for this purpose. The SEM and EDS were investigated at the end of the work because the carbon coating would contaminate the pellets.

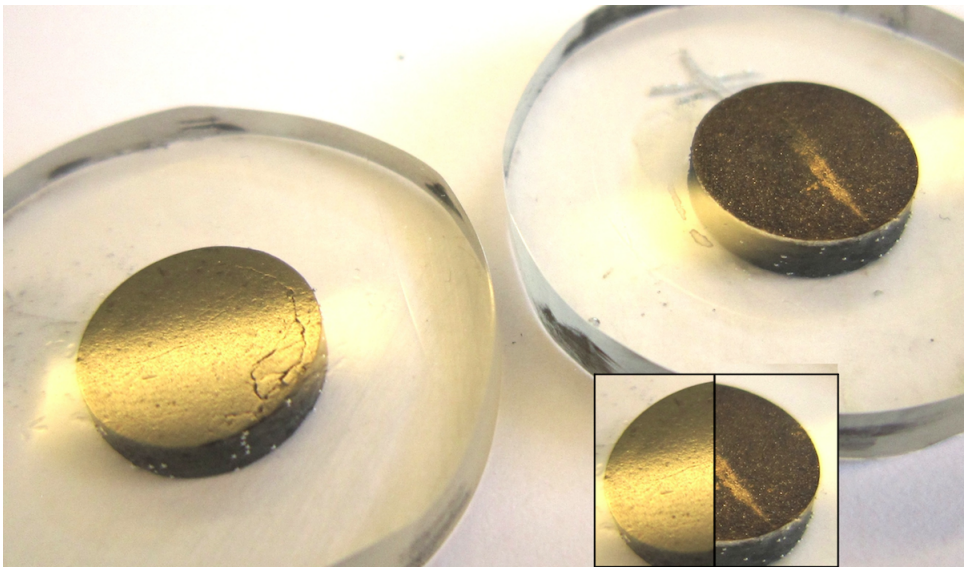

Figure 8: This image, taken with a handheld camera, shows clearly the different structure of the pellet surface of a polished sample of x= 0.25 (left) and a parallel sample after electrochemical measurements. The AFM data from section 4.2 is taken from these samples

Figure 9: This figure shows how the pellet samples are mounted to the sample holder. Colloidal solved silver is added between the copper contact and the pellets backside in order to ensure good electronic contact.

4 Results

4.1 Powders

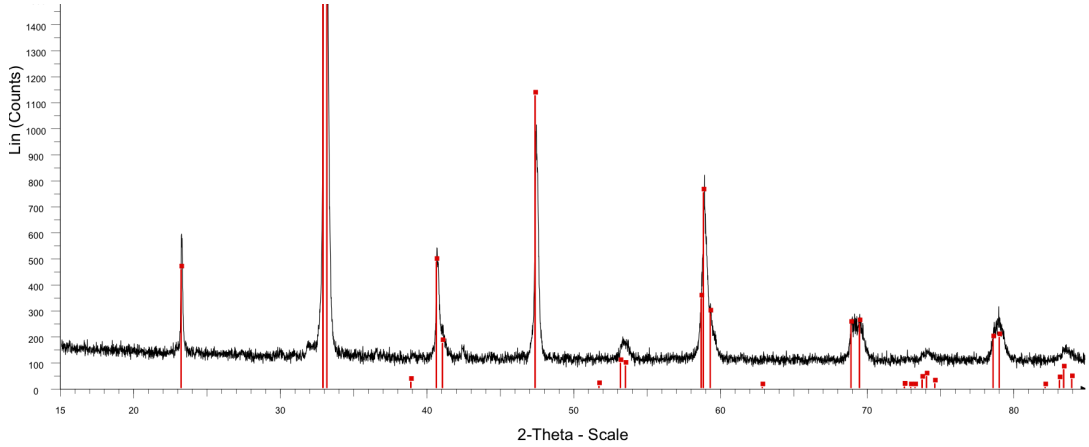

Figure 10: XRD of the sample containing x = 0.25. The vertical red lines are for a sample of $La_{0.75}Sr_{0.25}CoO_3$ from the XRD database.

The x = 0.25 sample were initially produced to investigate whether the method for producing powders resulted in satisfying qualities. Figure 10 shows that the XRD pattern matched with the $La_{0.75}Sr_{0.25}CoO_3$ from the database and that the sample consisted of the right phases and had the correct structure.

The successful XRD of x = 0.25 lead to approval of the synthesis quality, and the other samples were produced. The later XRD patterns showed that both the x = 0 and the x = 1 samples matched their individual patterns, but for the x = 0.5 and the x = 0.75 samples, a phase containing only Sr, Co and O were observed. This phase was only slightly visible in the x = 0.5 sample, but very evident for the x = 0.75 sample. This suggests that a pure $SrCoO_3$ phase is present which also implies that the LaSrCoO phase contains less strontium and more lanthanum than the stoichiometric value of 0.75.

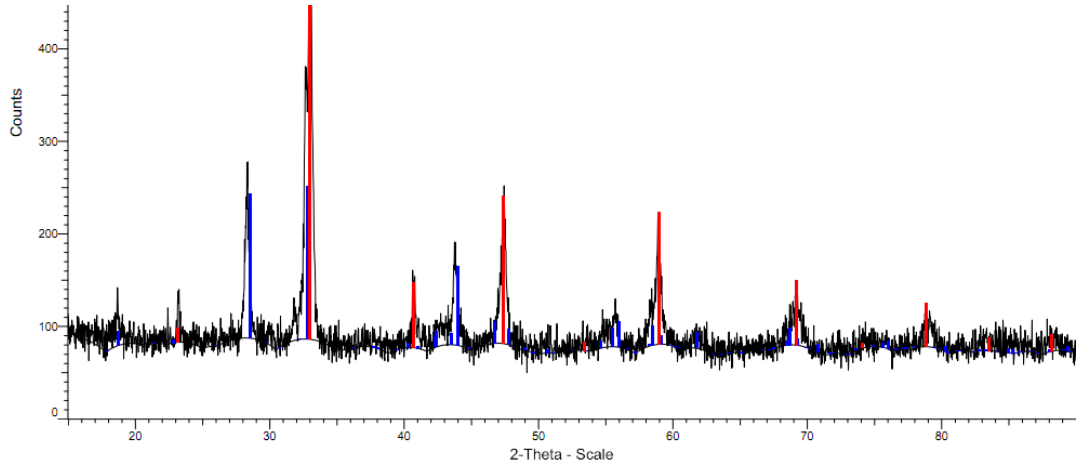

Figure 11: XRD of the sample containing x = 0.75. The vertical red lines are for a sample of $La_{0.25}Sr_{0.75}CoO_3$ and the blue lines represent SrCoO from the XRD database.

4.2 Pellets

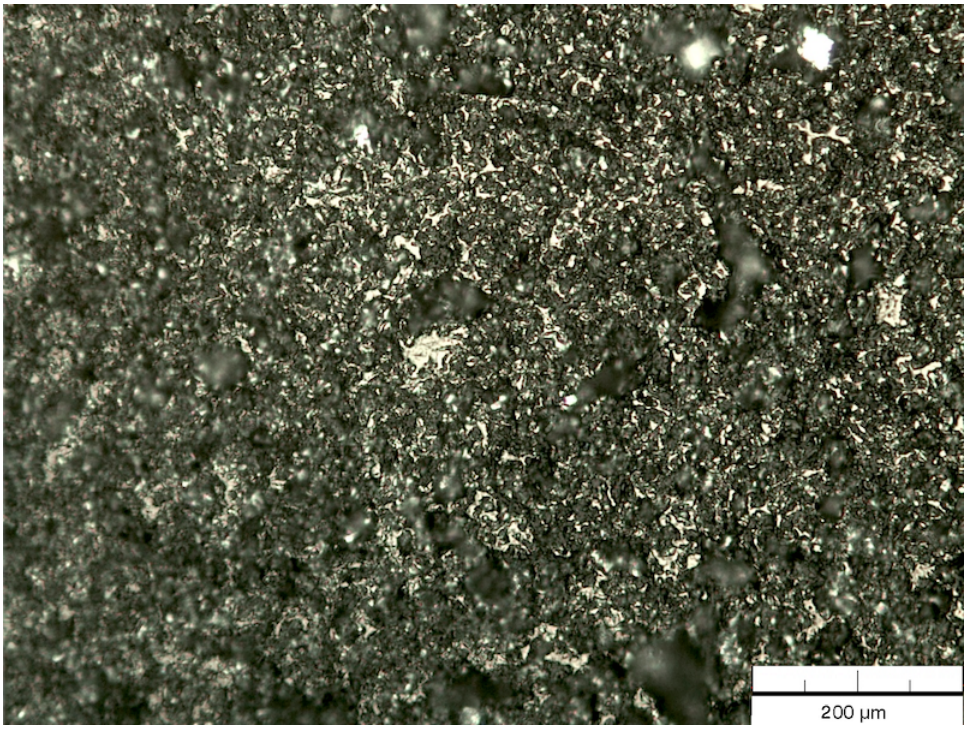

Figure 12: Light microscope image of the x = 0 sample after electrochemical testing with 50 x 1000 Magnification.

Light microscope images were taken of each sample aftee experimental testing. Figure 12 is a picture taken at high magnification with quite low depth of field. The image is focused at the bottom level and the many blurred spots are tops. This indicates a very rough surface due to corrosion. Comparing all the images in figure 13, the x = 0 and the x = 1 samples are the least corroded samples. The x = 0.5 sample has the roughest topography.

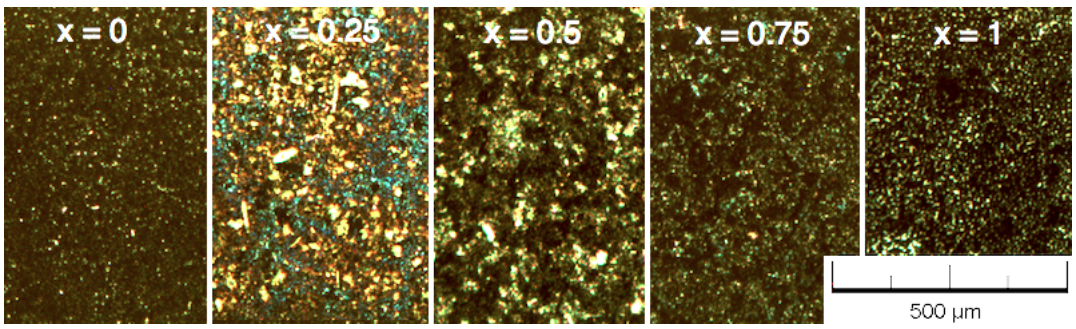

Figure 13: Light microscope images of all the samples with 20 x 1000 Magnification.

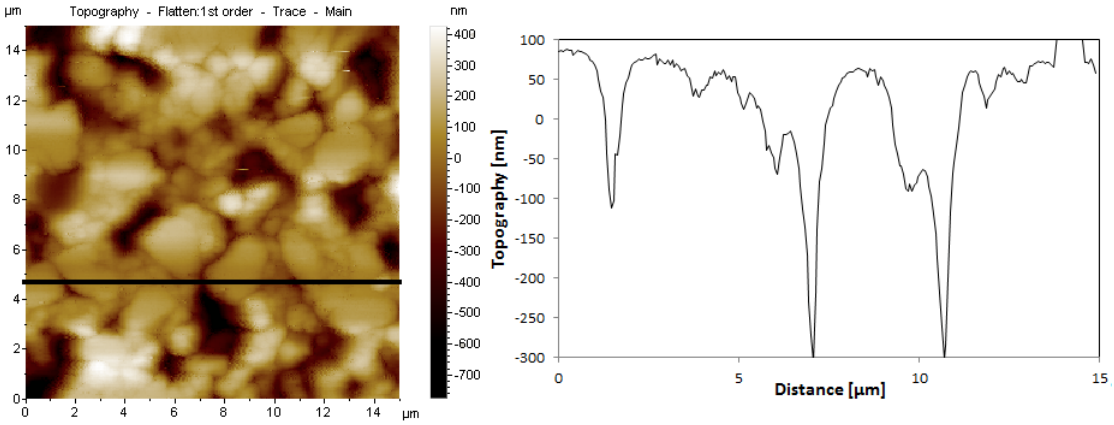

Figure 14: AFM image of the polished sample of x = 0.25 in figure 8 (left). The roughness can be seen from the cross-section.

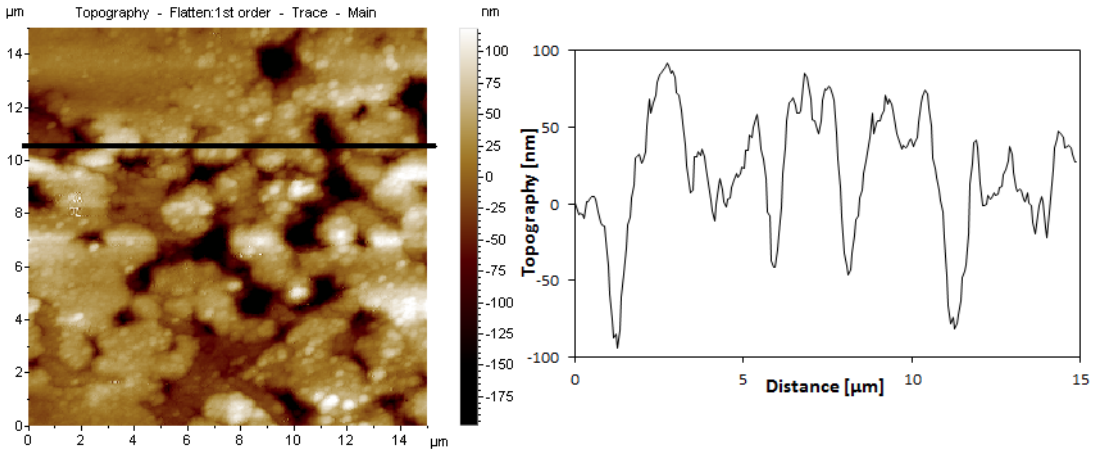

Figure 15: AFM image of the electrochemically tested sample of x = 0.25 from figure 8 (right).

Figure 14 reveal that the pellet sample had high porosity already before undergoing electrochemical experiments. Figure 15 seems to have a rougher topography. The cross-section from figure 15 were taken where no huge cracks were present in order to visualize the more low-frequent topography that occurs after testing.

After the final electrochemical testing, some of the samples were prepared for SEM imaging and EDS bulk measuring. The backscatter detector was unfortunately out of order so phases at the surface could not be identified. This was unfortunate because studying phases at the surface were of interest in order to understand both the quality of the synthesized product and how the electrochemical testing had affected the surface. It did also not allow for accurate composition measurements of single phases, and only bulk measurements were taken. Only three samples were imaged because of lack of time and supplies. These bulk compositions are presented in table 3.

Table 3: Composition at the surface after electrochemical testing measured by EDS. Compositions normalized so that the sum of La and Sr is 1.

	x = 0	x = 0.25	x = 0.75
La	1	0.82	0.41
Sr	0	0.18	0.57
Co	0.94	0.99	1.77
O	2.36	2.55	5.75

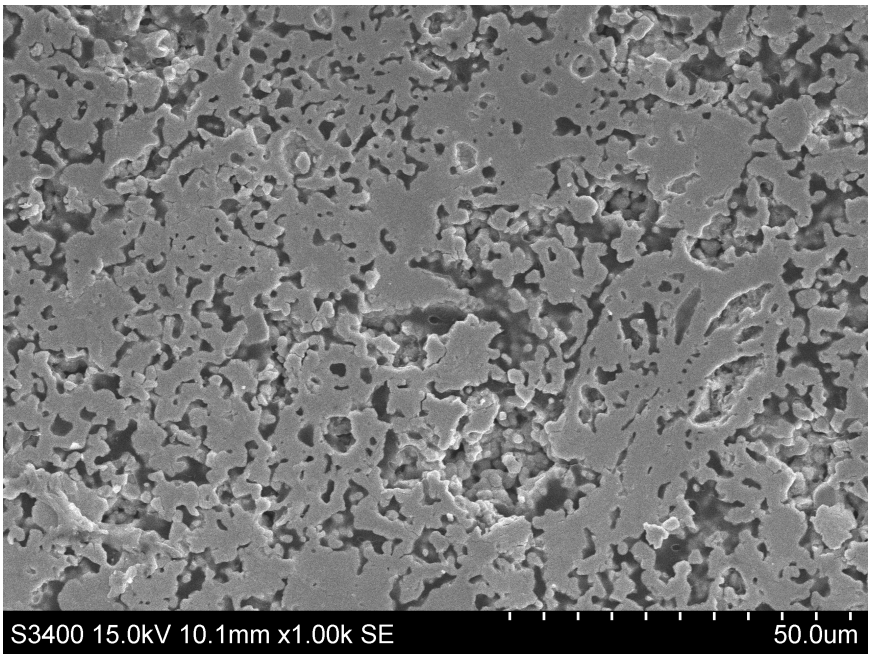

Figure 16: SEM image of x = 0.25 after electrochemical testing and magnification = 1k.

The surface concentration of oxygen was lower than 3. This was expected because the typical δ values in $La_{1-x}Sr_xCoO_{3-\delta}$ is about 0.5. The surface of x = 0.75 had large amounts of cobalt and oxygen in it, which indicates the presence of cobalt oxide. The SEM images shows much porosity in all the samples. SEM image of x = 0.25 is given in figure 48. Images of x = 0 and x = 0.75 can be found in the appendix.

4.3 Cyclic Voltammetry

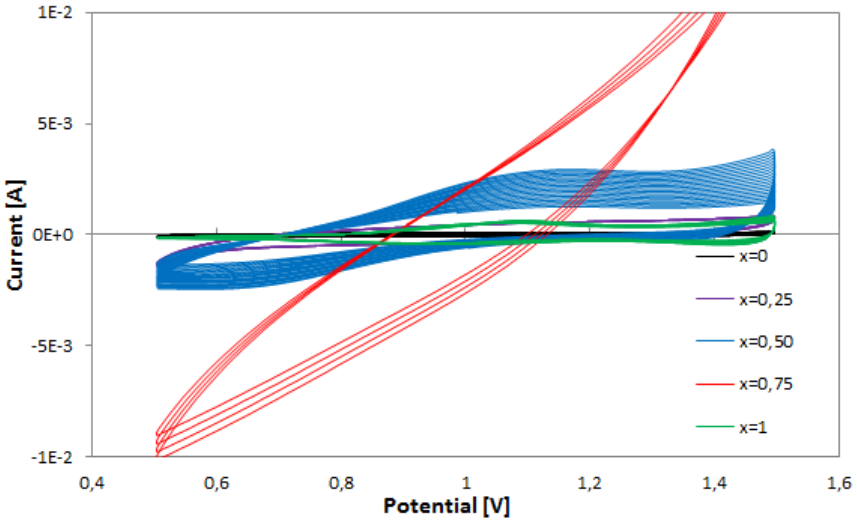

Figure 17: Cyclic voltammetry for all the samples. Scan rate: 20 mV/s. Only a few cycles are presented in the figure for the x = 0.75 sample in order to avoid overlapping.

The cyclic voltammetry (CV) results for all the electrodes are displayed in figure 17. In order to show the curves with lower current density, figures with increased resolution are given in figure 18 and 19. The CV shows how clearly how the electrochemical activity rises with each cycles. Especially x = 0.5 had a marked and constant increase in current density with each cycle, but this was also evident for the other samples. Figure 19 shows an increase in current only up to a certain point. That the rise in current slowed down with each sweep was also the case for most of the samples. This indicates that the corrosion process is slowing down when exposed to the same potential variations.

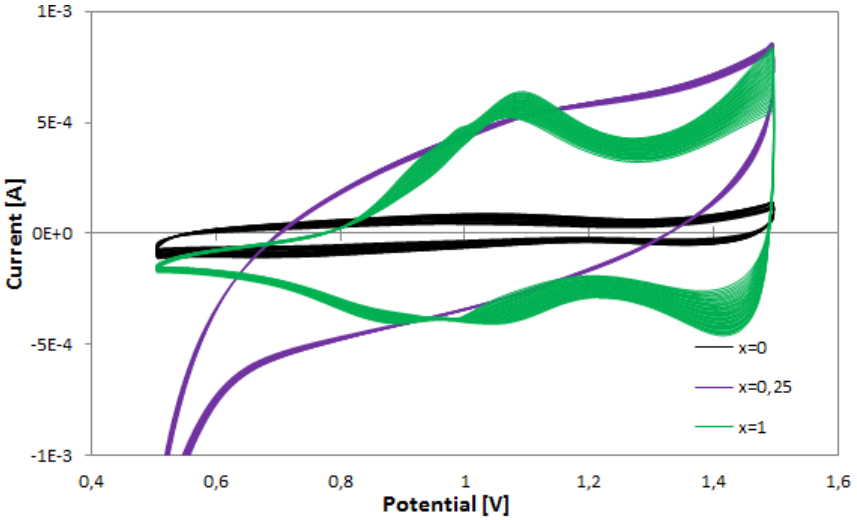

Figure 18: Higher resolution of figure 17. Scan rate: 20 mV/s.

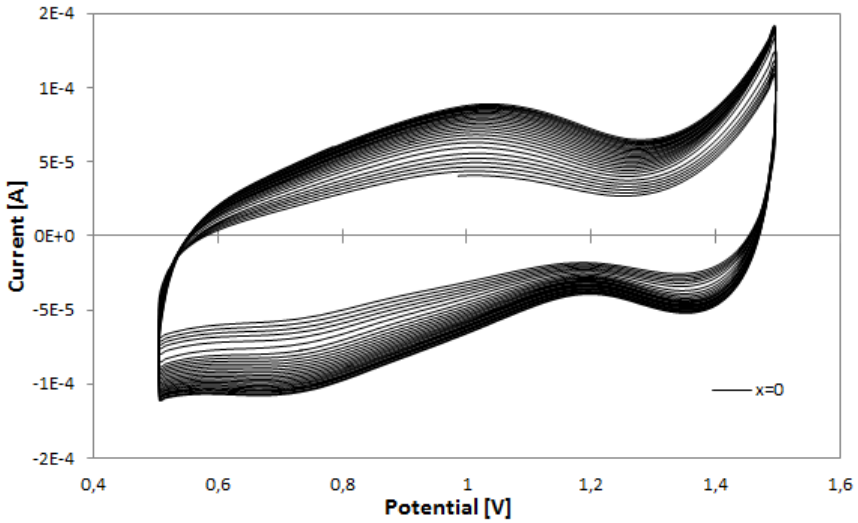

Figure 19: Higher resolution of figure 17. CV of $LaCoO_3$. Scan rate: 20 mV/s.

The electrodes showed an anodic and a corresponding cathodic peak prior to the onset of oxygen evolution, with the exception of x = 0.75 and x = 0.25. This is equivalent to the findings of *Singh* et al. [12] except that the peaks in this work are wider, and in the case of x = 0.75, not evident at all. The reason for this phenomena can be that these CV are done on pellet surfaces where many crystal orientations and maybe the presence of other phases will broaden the peaks. This statement is supported by noticing that the peaks for x = 0 and x = 1 are more distinct than for the samples with both lanthanum and strontium.

4.4 Polarization curves

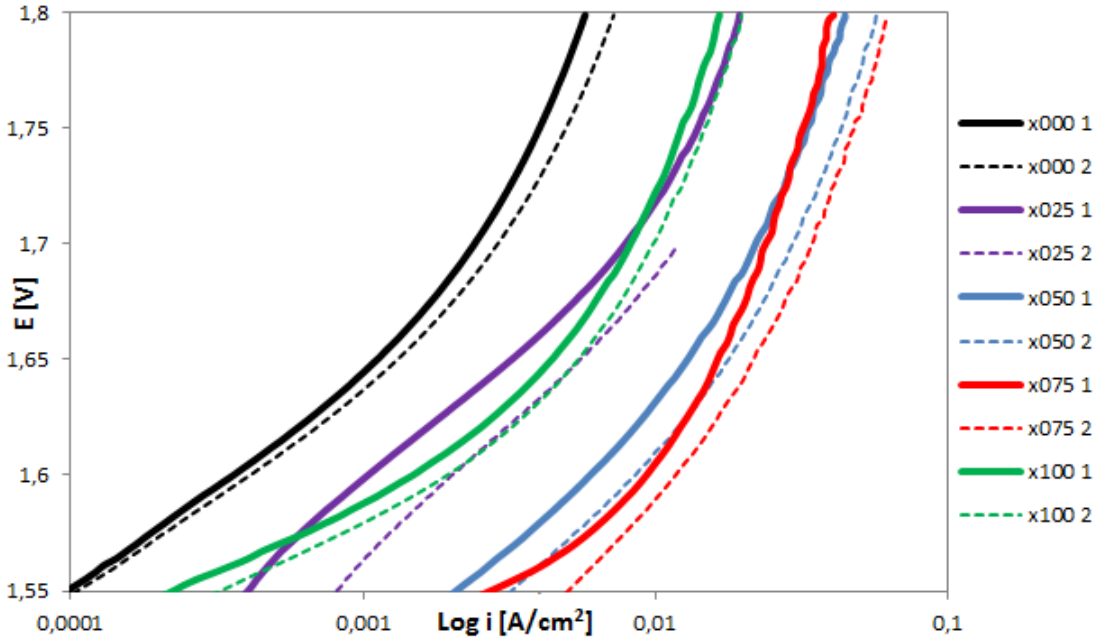

Figure 20: Stationary potentiostatic polarization curves after anodization. The full lines are for the initial measurement while the dotted lines are for a second measurement. Scan rate: 0.5 mV/s.

As the corrosion led to an increase in the surface area, two polarization curves were measured for all the samples. The first polarization curve was measured right after the initial CV as shown in figure 7. The second polarization curve was measured after extensive measuring. This would typically include a few CV and impedance measurements, but could vary from sample to sample.

The data for these curves have not been compensated for ohmic drops in the solution. The potential measured are therefore:

$$E = \eta + IR \tag{9}$$

Finding the resistance can be done by extending the linear region of the polarization curves and plot the potential difference (E_1-E_2) versus the current. This is illustrated in figure 21 A resulting linear curve going through the origin will confirm that the curvature is due to ohmic drops only. At higher current densities, oxygen evolution will cause formation of gas bubbles on the surface which again disturbs the current flow.

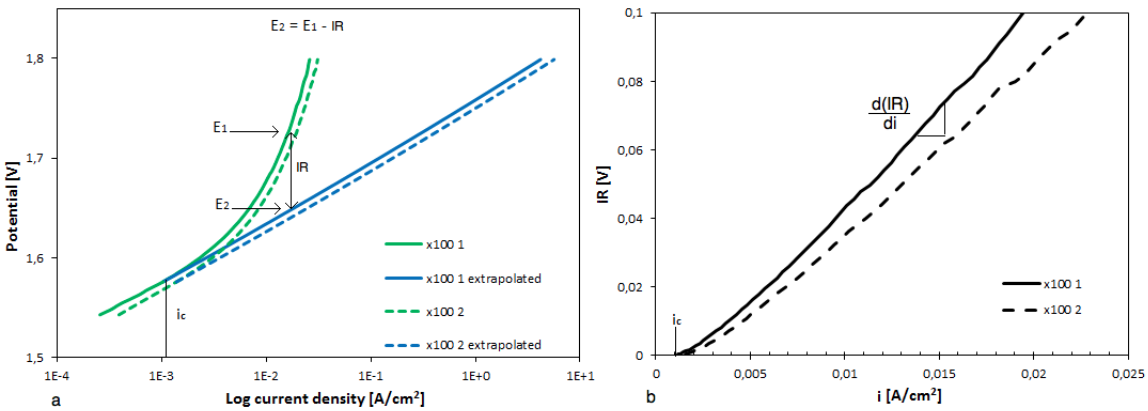

Figure 21: a: Polarization curves and Tafel lines for polarization measurement 1 (full lines) and 2 (dotted lines) for $SrCoO_3$. b: Plot showing the potential drop versus current of measurement 1 and 2.

The resistance was calculated from the slope of the IR-i curves. Plotted versus current, the slope is given by the resistance, but plotted versus current density, the slope is the product of resistance and surface area, R·A. The overpotential was calculated by:

$$\eta = E - IR = E - i\frac{d(IR)}{di} = E - iRA \tag{10}$$

Tafel lines where then found from the corrected curves as shown in figure 22

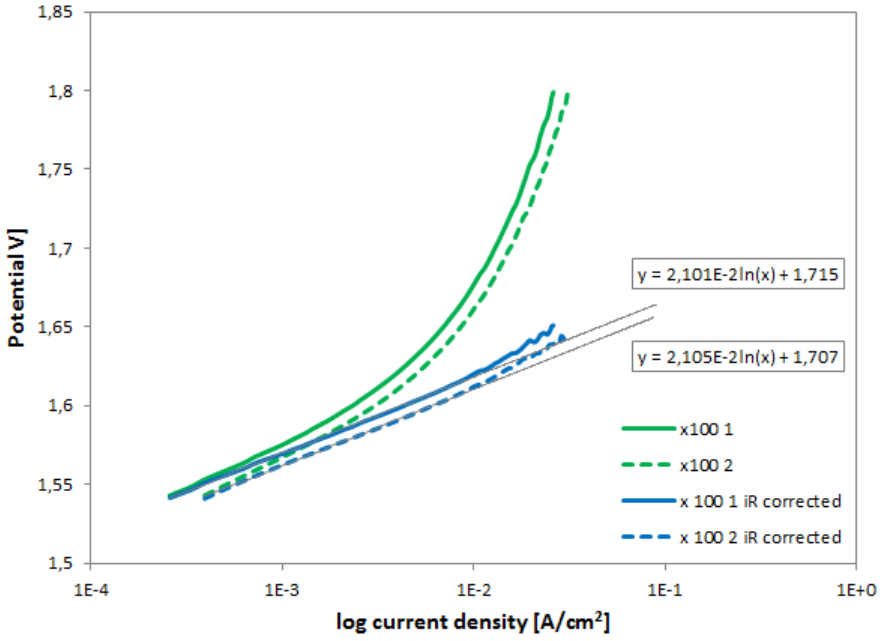

Figure 22: Polarization curves for the uncorrected and the corrected data. Tafel lines are found from the corrected curves.

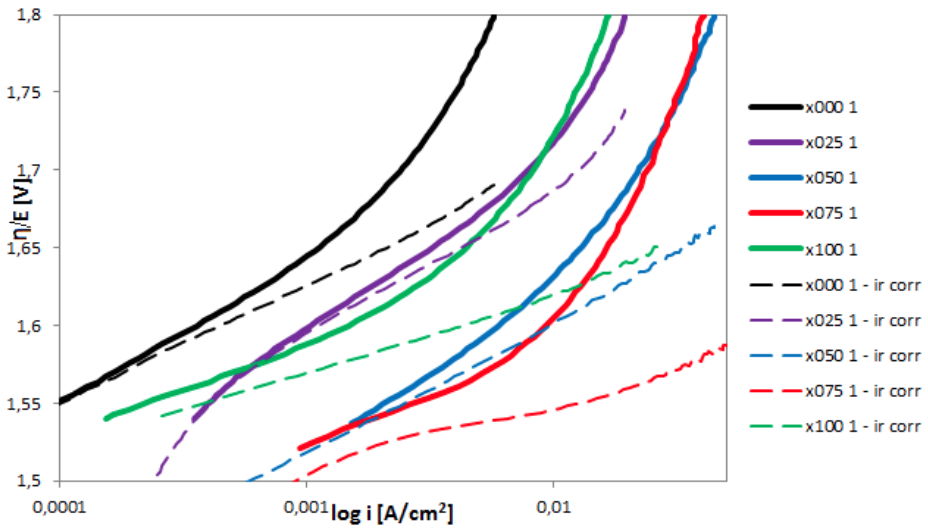

Figure 23: IR-correction of the first polarization curves. Full lines: uncorrected polarization curves. Dotted lines: IR corrected polarization curves.

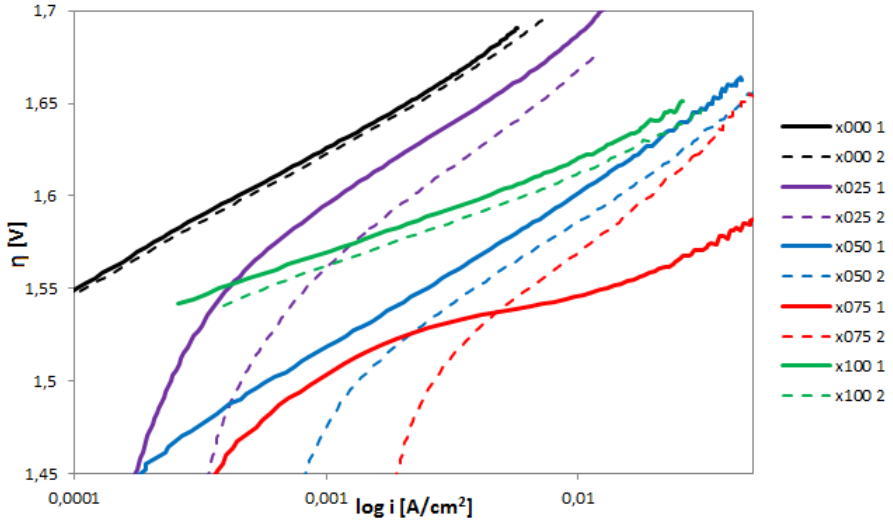

Figure 24: IR-corrected polarization curves of the first (full lines) and second (dotted lines) measurement.

Table 4: Ohmic resistances, Tafel slopes and the exchange current densities for first and second polarization curves.

	x = 0	x = 0.25	x = 0.5	x = 0.75	x = 1
R 1 [Ω]	11.99	1.98	1.93	2.07	3.62
R 2 [Ω]	9.21	1.20	1.50	1.29	3.14
b 1 [mV/decade]	78	87	85	45	48
b 2 [mV/decade]	78	103	93	106	48
i_0 1 [mA/cm^2]	$7.8{\cdot}10^{-9}$	$5.9{\cdot}10^{-8}$	$4.2{\cdot}10^{-7}$	$7.9{\cdot}10^{-10}$	$9.3{\cdot}10^{-11}$
i_0 2 [mA/cm^2]	$9.4{\cdot}10^{-9}$	$5.7{\cdot}10^{-7}$	$1.5{\cdot}10^{-6}$	$6.1{\cdot}10^{-6}$	$1.4{\cdot}10^{-10}$

The Tafel values shows in general an increase in the Tafel slope values for the first and the second measurement with exception of x = 0 and x = 1 which seems to be very stable. For x = 0.75 was the change in Tafel slope and for exchange current density very large. The first measurement for x = 0.75 has characteristics which compares best to x = 1, but the second measurement share characteristics with the other samples.

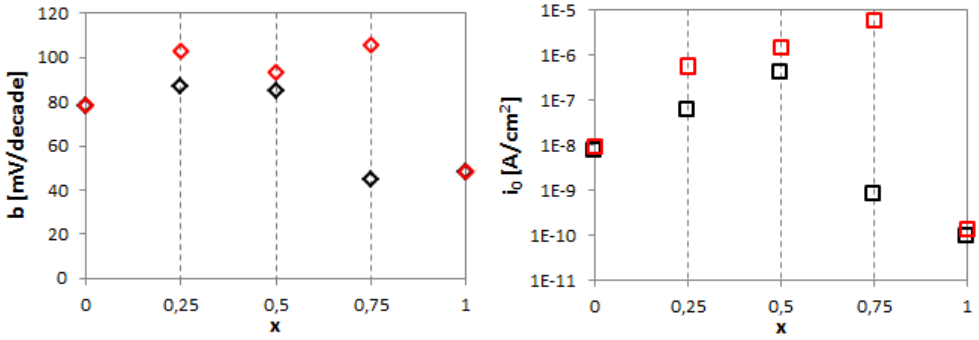

Figure 25: (a) Tafel slope and (b) exchange current density values from table 4. Black and red markers represent the first and the second measurements respectively.

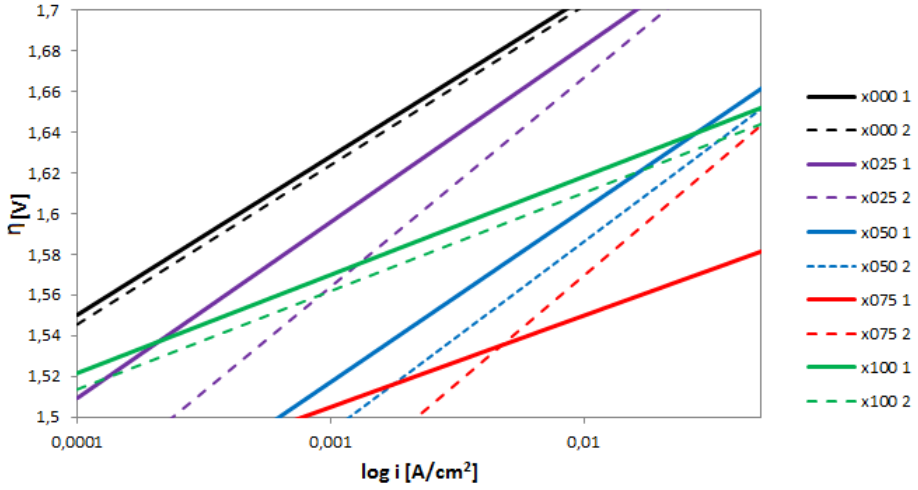

Figure 26: Tafel curves given in a E/log(i)-diagram.

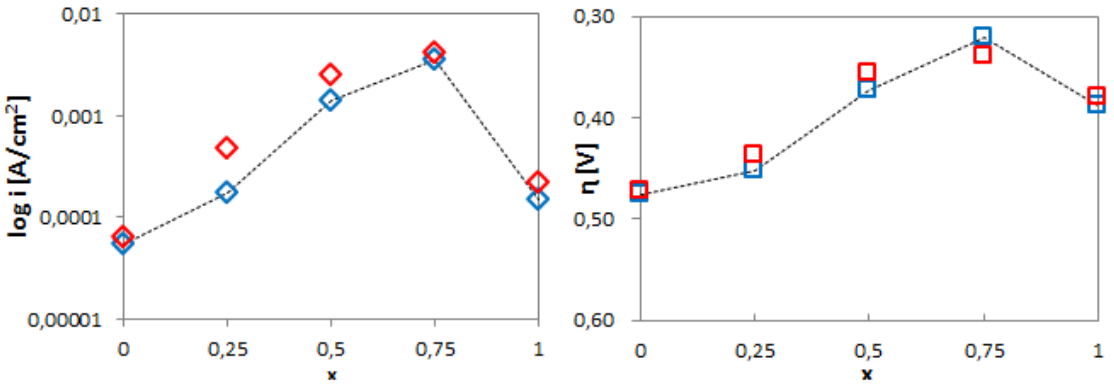

Figure 27: a: Current density at 0.3 V overpotential (1.53 V). b: Overpotential at current density 10mA/cm^2. Blue and red markers represent the first and the second measurements respectively. All values are calculated from the Tafel lines.

From the Tafel equation we get that low b-values combined with large i_0-values results in high current density. The general trend is that the x = 0.75 sample has the best catalytic properties followed by the x = 0.5 sample. Oxygen evolution starts at a high potential for the x = 1 sample, but due to the low Tafel slope, the catalytic activity at is better higher potentials.

The difference in the first and second measurement of the x = 0.75 sample makes it difficult to compare the electrodes with one another, as done in figure 27. This is solved by choosing to compare current density values at 1.53 V (η = 0.3 V) and compare the overpotential needed to get to 10 mA/cm^2. At these values, both the first and second measurement for x = 0.75 are very similar.

4.5 Double layer capacitance

The surface changes and the increase in the electrocatalytic activity with electrochemical testing were suspected to be an effect of increased surface area. The double layer capacitance, C_{DL}, was investigated as an increase in surface are will also lead to an increase in C_{DL}. The goal was to see if the polarization curves could be normalized with respect to the C_{DL} values.

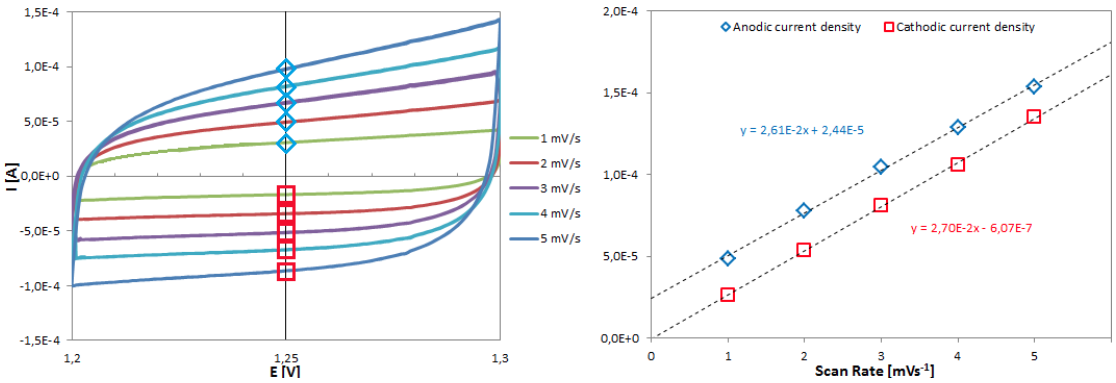

Figure 28: Left: Cyclic voltammetry of $La_{1-x}Sr_xCoO_3$ after the second polarization measurement from potential 1.2 to 1.3 V with different scan rates. Blue diamonds mark the anodic current density and red squares mark the cathodic current density. Right: The current densities are plotted versus sweep rate.

Figure 28 shows five CV for the x = 0.5 sample. The ideal curves should be as square as possible, but this was not the case, as the sample did not have a totally passive potential region. The curves showed a slight increase of current density, but more so for the anodic than for the cathodic currents.

The current density values at 1.25 V makes a straight line when plotted versus the sweep rate. The slope equals the capacitance of the sample. As the current densities for the anodic current had a tendency to vary more, the capacitance derived from the cathodic current densities were judged to be more accurate. In figure 29, the C_{DL} values for each sample after the first and after the second polarization curve are plotted. The values are very similar to the current density values for high potentials, see figure 27.

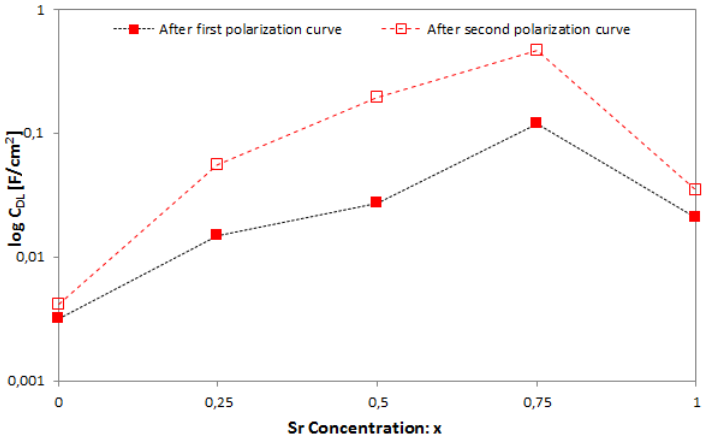

Figure 29: Double layer capacitance values measured from the cathodic current densities as shown in figure 28. The full line is for the first measurement, and the dotted line is for the second measurement.

The increase in C_{DL} is quite significant, and the increase is much higher for the highly doped samples than for the samples with only strontium and lanthanum. This result is not accurate as the amount of measuring and the amount of corrosion varied between the first and the second polarization curve for the different samples.

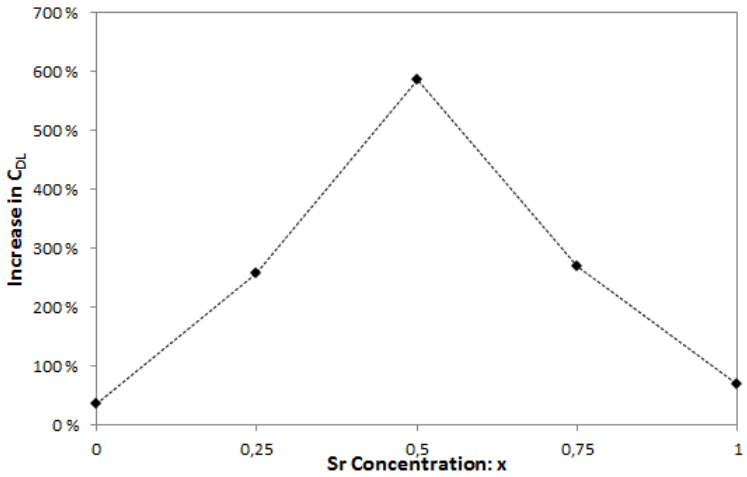

Figure 30: This figure illustrates how much the C_{DL} value have increased from the first to the second measurement. This figure indicates the corrosiveness of the different samples.

4.6 Charge Carrier Density

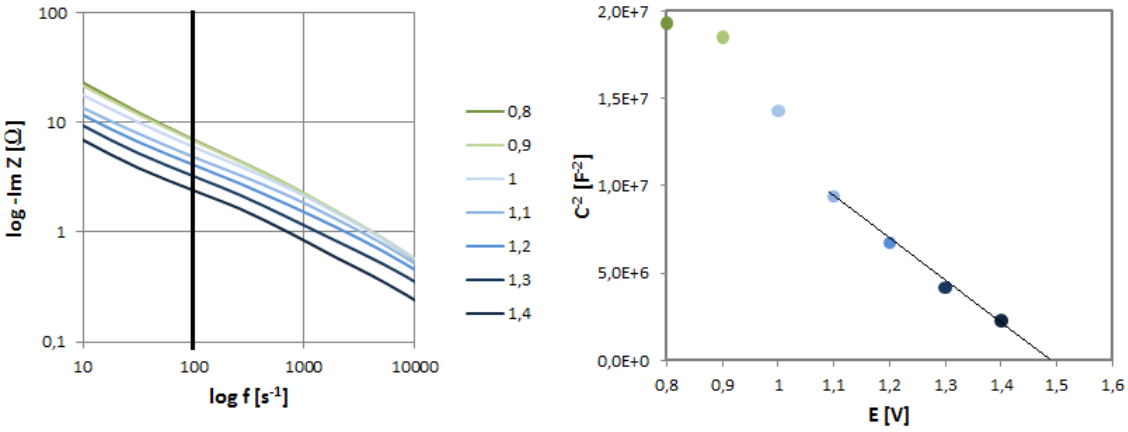

Figure 31: The right figure shows one of the impedance measurement for the x = 0.25 sample. Here the imaginary frequency is plotted versus frequency in a log-log diagram. Taking the values for a frequency (illustrated here for 100 Hz) and using them to find $\frac{1}{C^2}$ (by using equation 5) results in a Mott-Schottky plot (left figure). The slope of the approximated linear curve is given by the MS-equation (equation 6) and intersects at the flat-band potential.

The Electrochemical Impedance Spectroscopy (EIS) measurements were carried out from a potential range of 1.4 to 0.4 after ten minutes of anodizing at 1.4 V. The capacitance was derived from equation 5 and Mott-Schottky plots were constructed as illustrated and described in figure 31. For each MS plot, linear slopes were constructed, and some slope values are given in figure 33 and the flat band potentials are given in table 5. The MS plot for x = 0.75 is given in figure 32 and shows data and slopes for a few frequencies. MS plots for the other catalysts can be found in the appendix.

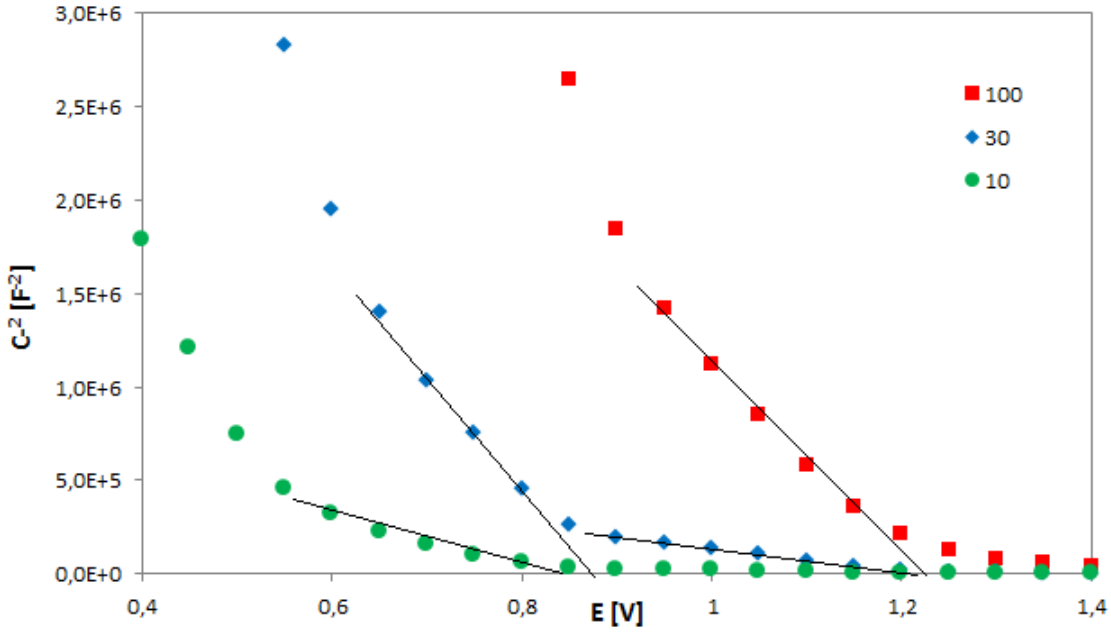

Figure 32: MS plot for x = 0.75 and frequencies 10, 30 and 100 Hz. The curves have two possible linear approximations and two V_{fb} and slope values.

The MS plot for sample x = 0.75 and x = 1 had two possible locations for the flat band potential. This behavior is typical for a two-phase substance. One at lower potential (0.8 - 1.0) with a steep slope and one at higher potential (1.4 - 1.7) with a less steep slope. The higher potential V_{fb}s and their slopes are given in figure 33 and were used for comparison with the other samples. Reason being that the V_{fb}s for the other samples were located in the same potential region, see table 5.

Table 5: Flat band potential for the samples

	x = 0	x = 0.25	x = 0.5	x = 0.75	x = 1
V_{fb}[V] low E	-	-	-	0.9	0.95
V_{fb}[V] high E	1.45	1.45	1.45	1.25	1.7

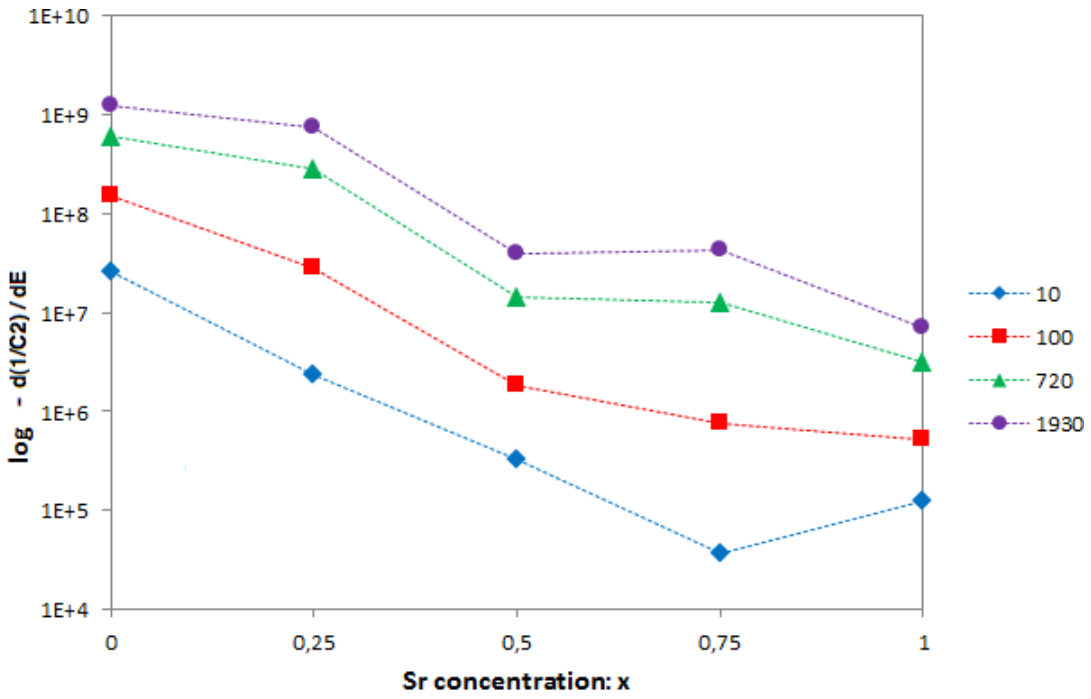

Figure 33: Slope values $(-\frac{d(\frac{1}{C_D^2})}{dV})$ from the MS plots for four different frequencies. The slope values equals $\frac{2}{\epsilon\epsilon_0 A^2 e N_A}$. The reason for the minus sign is because the MS slope is negative for a p-type conductor where acceptors are the major charge carriers. This results in using N_A in the MS equation and not N_D.

The general trend of the slope values in figure 33 is that the slope decreases with increasing strontium concentration. This result adds up as the slope is inversely proportional to charge carrier density (see equation 6) and the amount of acceptors increases with doping. The slope also depends on surface area and permittivity, so deviations occur. Surface area varies with the amount of corrosion, and permittivity varies with frequency, doping concentration and sintering procedure.

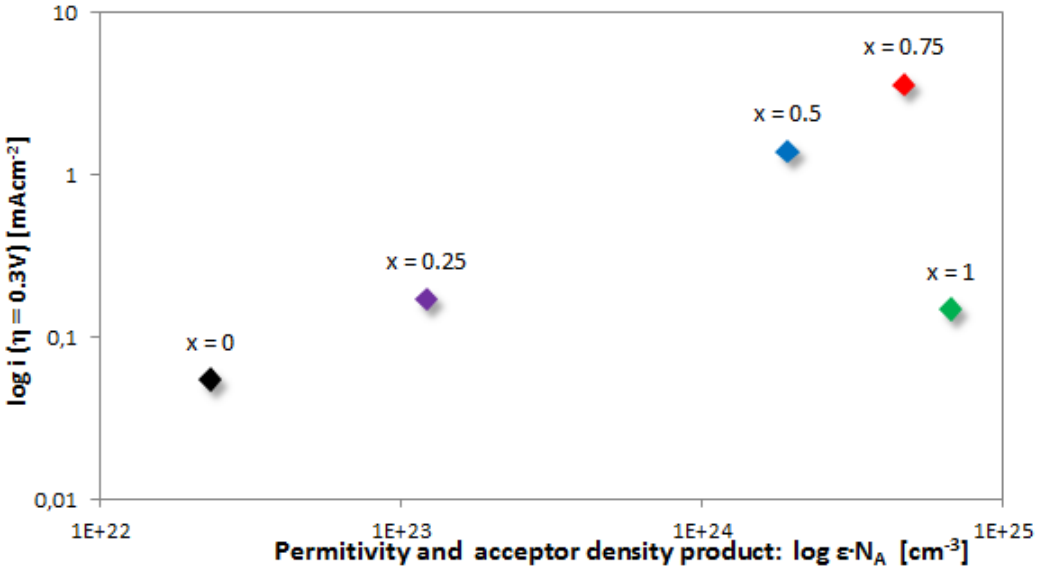

Figure 34: Plot of current density at 0.3 V overpotential versus permittivity and acceptor density product in a log-log diagram.

A relation between the current density and the charge carrier density be established by using the data from the polarization curves and from the MS plots. Such an attempt is presented in figure 34 where the current densities for the first polarization measurement at 1.6 V from figure 27 is plotted versus the product of permittivity and acceptor density product. This product is calculated from the slope values at 100 Hz from figure 33 and using equation 7.

5 Discussion

5.1 Sample preparation

The chosen procedure for sample preparation was the solid-state synthesis, which is a relative simple procedure. This can lead to large particle size, which again could lead to high porosity in the pellets. XRD indicated the presence of a $SrCoO_3$ phase in the x = 0.75 sample, and EDS indicated the presence of a CoO_3 phase. whether the origin of these phases are caused by the synthesis, the sintering or the experimental procedure is uncertain. It is, however, certain that these phases are unwanted. Repetition of the milling and calcination steps might have helped to minimize particle size and also helped towards a more complete synthesis and a more homogenous material.

The samples risked cracking while being mounted into the sample holder. Such a crack was observed in light microscope for the x = 0.5 sample, which may explain to some extent why the corrosiveness of this sample was so much larger than for the other samples. Caution must therefore be applied when mounting the samples.

The pellets were all calcined and sintered at the same temperatures. The choice of sintering time and temperature were largely affected by the availability of the ovens. The optimal calcination and sintering temperature is likely not the same for the different samples and will most likely vary with composition. *Kleveland* et al. [6] showed that for 2 hours of sintering, the temperature needed for optimal density for $LaCoO_3$ is $\geq 1350\,^{\circ}C$ but sinks to $\geq 1200\,^{\circ}C$ for $La_{0.8}SR_{0.2}CoO_3$. *Kleveland* also reports of higher density for $LaCoO_3$ sintered at $\geq 1200\,^{\circ}C$ for 20 hours than for 5 hours, but $La_{0.8}Sr_{0.2}CoO_3$ were largely unaffected by sintering time. Based on this, assumed different preparation methods doesn't affect the parameters, the sintering time could therefore be longer or the temperature higher for the x = 0 sample. The sintering time and temperature of the x = 0.25 sample on the other hand, should have been close to optimal. The SEM images suggests that the density were a little better for x = 0.25 than for x = 0, but the porosity were still severe. Sintering time and temperature are likely not the most critical factor in deciding the porosity and the focus should be on powder production.

Investigation and understanding of the surface area topography and corrosion effects became two of the main focuses for this work. Denser samples would have made this effort either easier or maybe unnecessary . Effort should therefore be made to study and optimize the density of the samples.

5.2 Electrochemical characterization

In this work was the anodization process set to 1.4 V for 10 minutes. *Vondrak* et. al. [5] reported that they had to anodize at 1.4 V for 1 hour to fully reach a steady state. The polarization curves can therefore, to some degree, have been affected by not being at steady state. The ohmic resistance for x = 0 is higher than for the other samples, and is probably due to it not being a extrinsic semiconductor and therefore likely have higher resistance ($\sim 3\Omega$cm[1]) than the other samples. Bubbles were formed at the surface at high potentials, and some of these would remain on the surface even when going to lower potential. This would happen after the polarization and before measuring the C_{DL}. Tapping the mounting device would remove these, but a better way of reducing this possible source of error, could be to use a rotating disc electrode.

The sample with x = 0.75 changes its Tafel slope drastically from b = 40 to b = 80. This points towards a change in the rate-determining-step, but will not be elaborated on here. The cause of this change, can be selective corrosion. If one phase would corrode easier than the other, the surface would be free of this phase, and the characteristics would also change. As the Tafel Slope of $SrCoO_3$ were 40 mV/s, it can be speculated that it was this phase that have disappeared from the surface. Surface diffusion or other effects can also be the cause of this change.

5.3 P-type and N-type conduction

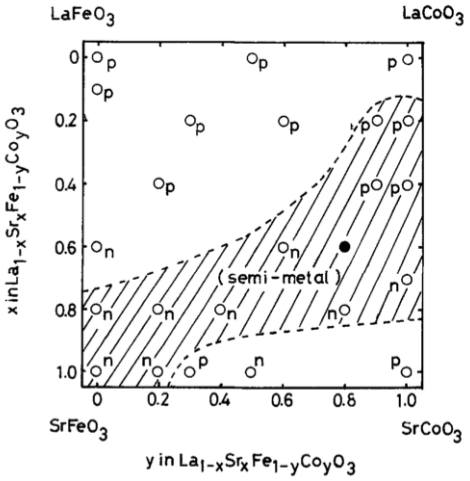

Figure 35: Shows how conduction type vary with different doping concentration. At the left side of the plot, y = 1, $La_{1-x}Sr_xCoO_3$ is found. P type conduction for all x except 0.75. [10].

From the work of *Matsumoto* et. al [10], a n-type conduction transition at around x = 0.75 was reported, figure 35. In this study, only p-type conductivity was discovered at potentials around the flat band potential. In the previous work [1], both types of conductivity was discovered for x = 0.4, depending on potential and pre-polarization. In this work, two Mott-Schottky plots were taken for the x = 0.75 sample in order to investigate this. One measurement pre-polarized at 0.2 V and the other at 1.4 V. A change in the slope from positive to negative was discovered for the cathodized curve at 0.2 V. This can mean that the type of conductivity can be manipulated by polarization.

The reason for the n-type transition not being observed at high potential can be because the x = 0.75 sample was not synthesized correctly, as discussed in 5.1.

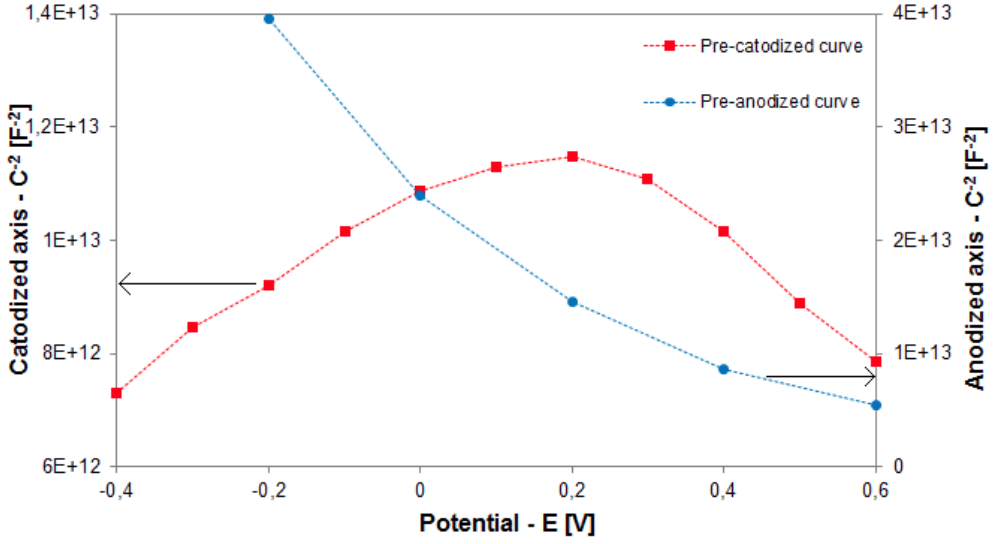

Figure 36: MS plot of x = 0.75 at 10kHz. The curve anodized at 1.4 V is blue and the red curve was cathodized at -0.4V. A negative slope indicates p-type conduction. The cathodized curve has a positive slope under 0.2 V indicating that the conduction here is n-type.

5.4 Oxygen evolution and charge carrier density

Comparing ϵN_A from figure 34 to the theoretical strontium concentration values in figure 37 shows that the values are almost in the same range The acceptor density, N_A, is closely related to the strontium concentration as every Sr-atom dopes with one hole. The ϵN_A values are in 2 orders of magnitude larger than the Sr-concentration, and the ϵN_A-axis is logarithmic. Four suspected contributing causes for these differences are: Firstly, the samples were not purely extrinsic. Especially for x = 0 which is an intrinsic semiconductor. The amount of charge carriers in x = 0 is therefore not 0. Secondly, the oxygen vacancies will p-dope the material. Thirdly, the relative permittivity has a typical value in the range of 1-10 and the ϵN_A value will therefore be larger than N_A. Lastly, the roughness has not been accounted for. This value range can typically be in the size of 10-100 and ϵN_A is proportional to A^{-2}, as shown in equation 14. This is discussed in the next section.

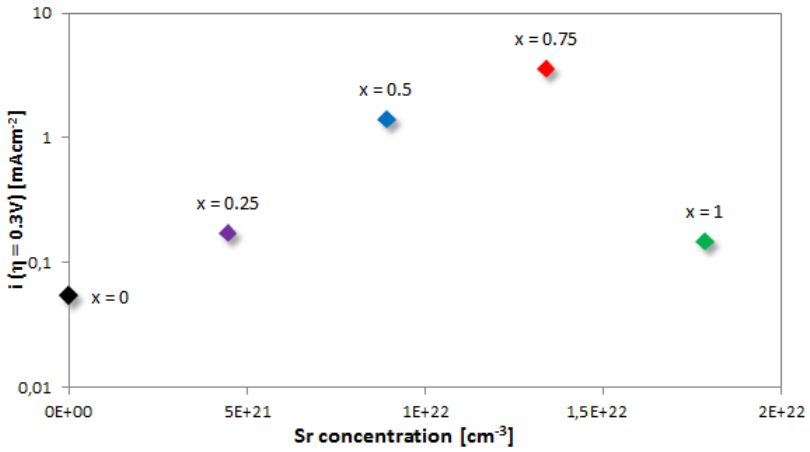

Figure 37: Current density at 0.3 V overpotential versus theoretical values of strontium concentration.

5.5 Normalization attempts

Corrosion challenged the task of finding the "true values" for the electrolytic properties as the results changed with time and measuring. Normalizing the results with respect to the surface roughness would give the best data, but the actual surface area was not found. Calculated roughness factors from the AFM data from figure 14 and 15 resulted in values of 1.131 and 1.025 for the pre- and post-experimental samples. These values are very low, and do not show an increase in the roughness as expected. The idea of normalizing the results with basis in the AFM data was dropped.

Another attempt was to normalize the surface area by finding the roughness factor σ based on the increase in double layer capacitance. The assumption was that the nominal double layer capacitance, C_{DL}, for a flat surface is 6 μF, and that an increase in surface area would lead to a linear increase in C_{DL}.

$$Atrue = A_{projected} \cdot \sigma \tag{11}$$

$$\sigma = \frac{C_{DL}}{C_{DL-nom}} \tag{12}$$

Here, $A_{projected}$ is the projected surface area (0.636 cm^2) and is the surface area used in all graphs presented in this work so far. Although this seemed reasonable, the resulting roughness factors scaled from 1'000 to 100'000, giving meaningless results.

In figure 34, the roughness is assumed to be that of a flat surface ($\sigma = 1$). As mentioned in section 5.5, the roughness will largely affect the results. If the area is assumed to be equal to $\sigma \cdot A$ where σ is the roughness factor, will σ change the values for current density and for ϵN_A as follows:

$$i = \frac{I}{A \cdot \sigma} \tag{13}$$

$$\epsilon N_A = \frac{dV}{d(\frac{1}{C_D^2})}(\frac{2}{\epsilon_0 e})\frac{1}{(A \cdot \sigma)^2} \tag{14}$$

5.6 Normalization attempt based on the increase in double layer capacitance

Finding a good assumption for the surface roughness was futile, but a decent attempt has been made here. The basis for this assumption is figure 30 and the increase in C_{DL}, not C_{DL} itself. If the roughness of the samples were initially the same, σ_0, and further corrosion is the only deciding factor of roughness, the roughness factor can be found by:

$$\sigma = (100\% + \%Corr)\sigma_0 \tag{15}$$

σ_0 were chosen to be 5. This value is not so important when comparing samples, as it will cause no relative change. The resulting roughness values are given in table 6. If these roughness values are used with equations 13 and 14, figure 34 will be corrected to give figure 38.

Table 6: Corrosiveness derived from figure 30 and σ values from equation 15

	x = 0	x = 0.25	x = 0.5	x = 0.75	x = 1
%Corr	35 %	257 %	587 %	270 %	69 %
σ	6,76	17,85	34,33	18,50	8,45

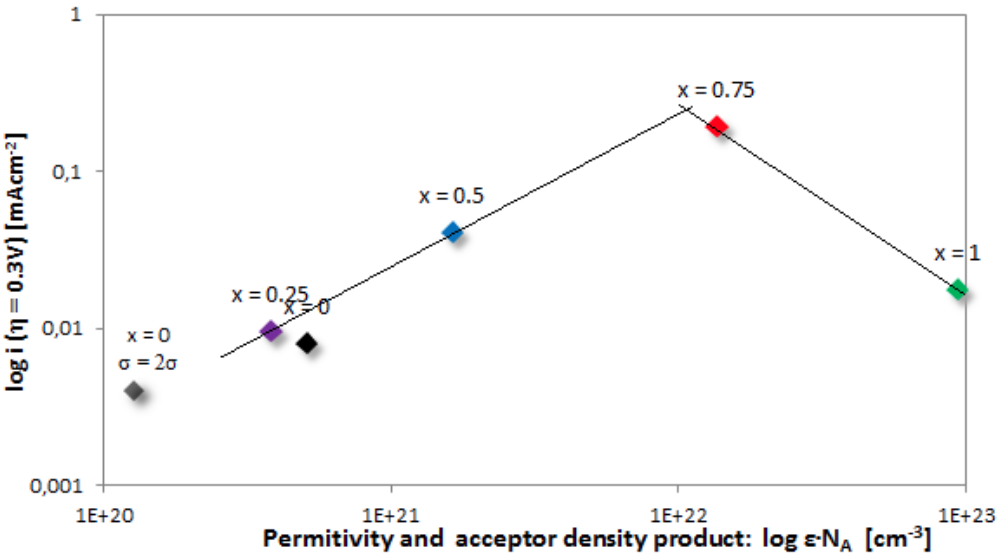

Figure 38: The assumed roughness factors from table 6 gives this relation of activity and acceptor density. The result can be interpreted as a volcano plot, but this can not be concluded due to lack of sufficient data points. For x = 0, two points are plotted, one with the same σ as the other samples and one with two times this value. This shows the increase necessary to get this data point lined up with the others.

Figure 38 shows a clear linear increase in current density with the increase in acceptor density up to x = 0.75. The activity decreases for the x = 1 sample. Further increase in charge carrier density could, based on this, lead to a decrease in activity. However, the x = 1 sample had very different characteristics overall, and this can not be said for certain.

By doubling the roughness factor for x = 0, it falls in line with the other samples. This can be justified by claiming that this sample had a greater initial roughness, caused by e.g. the sintering temperature not being as high as it should have been (discussed in section 5.1).

The work of *Vondrak* et. al. [5] report a $\epsilon E_A = 2.8 \times 10^{21} cm^{-3}$ for $La_{0.8}Sr_{0.2}CoO_3$ and an assumed roughness factor of 30. This is in agreement with the results presented in this work.

6 Conclusion and further work

The pellet surfaces were measured in alkaline solution, and Tafel equations and Mott-Schottky plots were successfully created. XRD and EDS showed that the sample compositions were almost as the targeted compositions. AFM, SEM and Light microscope imaging revealed a very rough surface.

The role of corrosion and roughness was much more important than predicted, and the synthesis and sintering procedures are therefore likewise essential. Electrochemical measurements on such corrosive material, require very careful sample preparation and optimal sample densities. Calculating and finding the sample roughness is important, but a working method for finding this in so corrosive samples is not known. It did not work to derive the roughness factors directly from the double layer capacitance.

The work in this rapport supports the theoretical hypothesis, with experimental data for the charge carrier densities, that the electrocatalytic activity increase with increasing charge carrier density. This was shown for $La_{1-x}Sr_xCoO_3$ up to x = 0.75, which had the highest activity among the samples.

The first challenge to overcome would be to find a procedure to produce pellets with better density and thus less corrosiveness. This procedure must also prevent unwanted phases in the samples. The second would be to find a way to control and measure the surface roughness of the samples. If this could be accomplished, reproducing this work would yield better and more conclusive results.

7 Acknowledgement

I wish to thank everyone who supported and encouraged me and my work.
Professor Svein Sunde for counsel and guidance.
PhD Candidate Anita Reksten for all help and guidance.
PhD Candidate Morten Tjelta for help at the laboratory.
Assistant Professor Lars Erik Owe for counsel and advice.
Staff Engineer May Grete Sætran for facilitation of my work.
Master student Stian Gurrik for reading correction and feedback.

References

[1] E. Bjartnes. Karakterisering av la(1x)srxcoo3 som katalysator til alkalisk vannelektrolyse. TMT 4500 Materials Technology, Specialization Project, NTNU, 2011.

[2] John O'M. Bockris. The electrocatalysis of oxygen evlution on perovskites. *J. Electrochem. Soc.*, February 1984.

[3] S. Trasatti C.P. De Pauli. Composite materials for electrocatalysis of o2 evolution: Iro2/sno2 in acid solution. *Journal of Electroanalytical Chemistry*, 2002.

[4] K. Gelderman L. Lee S. W. Donne. Flat-band potential of a semiconductor: Using the mott–schottky equation. *Journal of Chemical Education*, 84(4), April 2007.

[5] L. Dolezal J. Vondrak. The electic and electrochemical properties of electrode perovskite la1-xsrxcoo3. *Electrochimica Acta*, page http://www.sciencedirect.com/science/article/pii/0013468684870978, 1983.

[6] T. Grande K. Kleveland, M.-A. Einarsrud. Sintering of lacoo3 based ceramics. *Journal of the European Ceramic Society*, 2000.

[7] Matthew W. Kanan and Daniel G. Nocera. In situ formation of an oxygen-evolving catalyst in neutral in situ formation of an oxygen-evolving catalyst in neutral water containing phosphate and co2+. *Science*, 321(1072), 2008.

[8] Kia S. Wallwork Richard G. Haverkamp Svein Sunde Lars-Erik Owe, Mikhail Tsypkin. Iridium–ruthenium single phase mixed oxides for oxygen evolution: Composition dependence of electrocatalytic activity. *Electrochimica Acta 2012*, 2012.

[9] P. Bezdicka A. Wattiaux J. C Grenier M. Pouchard P.Hagenmuller. Preparation and characterization of fully stoichiometric srcoo, by electrochemical oxidation. *Z. anorg. allg. Chem.*, 619, 1993.

[10] Y. Matsumoto H. Manabe E. Sato. Oxygen evolution on la(1-x)srxcoo3 electrodes in alkaline solutions. *J. EIectrochem. Soc.*, 1980.

[11] Y. Matsumoto S. Yamada T. Nishida E. Sato. Oxygen evolution on lal sr felseries oxides. *J. Electrochem. Soc.*, 127(11), 1980.

[12] Ravidra N. Singh, Shashi K. Tiwari, Shri P. Singh, Narendra K. Singh, Gerard Poillerat, and Pierre Chartier. Synthesis of (la, sr)coo3 perovskite films via a sol-gel route and their physicochemical and electrochemical surface characterization for anode application in alkaline water electrolysis. *J. Chem. Soc., Faraday Trans.*, 92:2593–2597, 1996.

[13] Jin Suntivich. A perovskite oxide optimized for oxygen evolution catalysis from molecular orbital principles. *Science*, 334, 2011.

8 Appendix

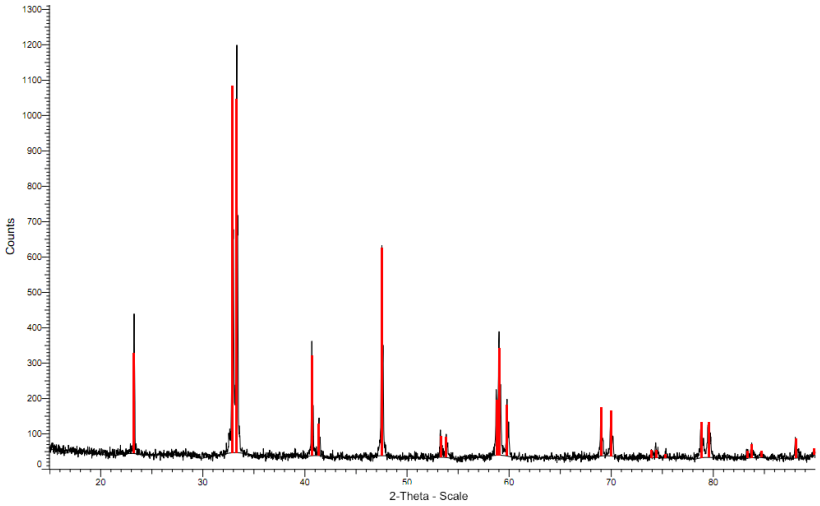

Figure 39: XRD of the sample containing x = 0. The vertical red lines are for a sample of $LaCoO_3$ from the XRD database.

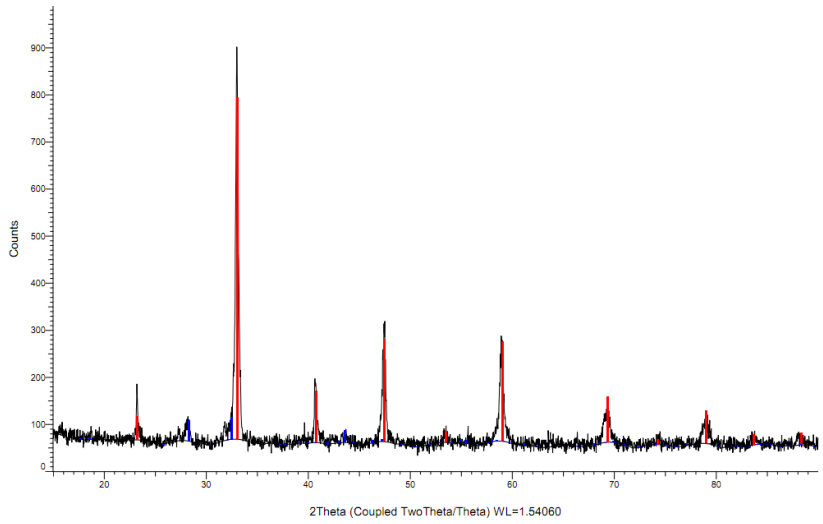

Figure 40: XRD of the sample containing x = 0.50. The vertical red lines are for a sample of $La_{0.5}Sr_{0.5}CoO_3$ and the blue lines represent SrCoO from the XRD database.

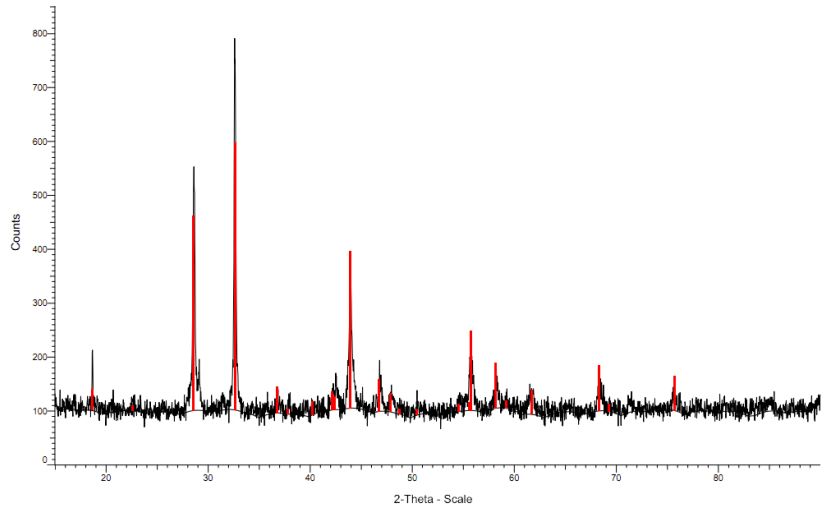

Figure 41: XRD of the sample containing x = 1. The vertical red lines are for a sample of $SrCoO_3$ from the XRD database.

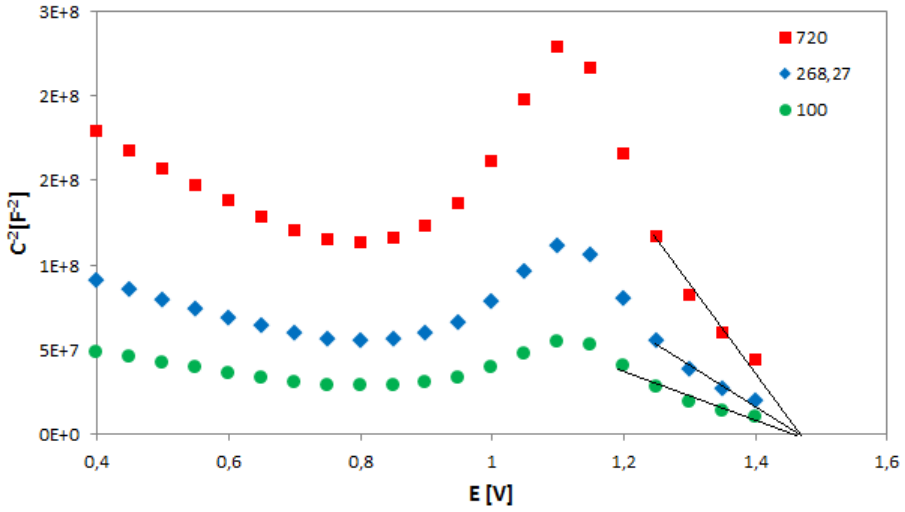

Figure 42: MS plot for x = 0 and frequencies 100, 268 and 720 Hz. The curves seems to have two possible linear approximations.

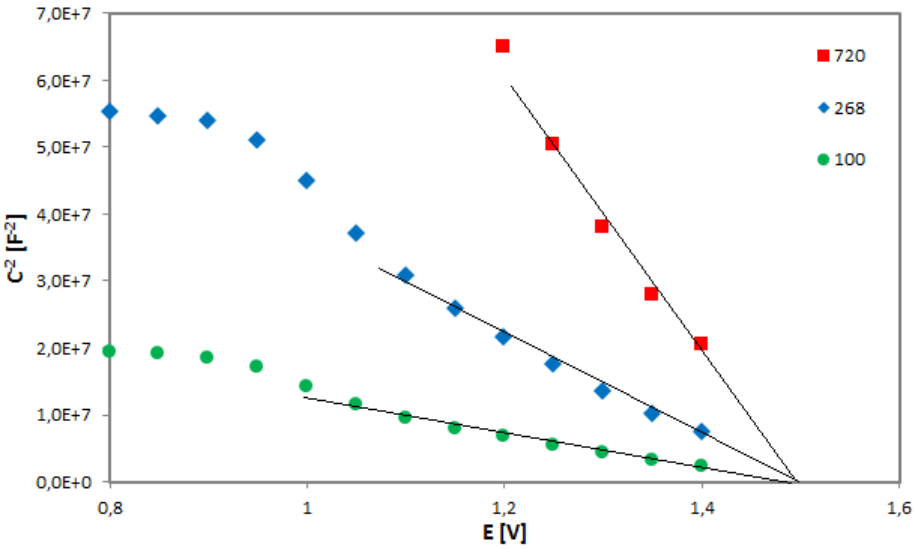

Figure 43: MS plot for x = 0.25 and frequencies 100, 268 and 720 Hz. The curves seems to have two possible linear approximations.

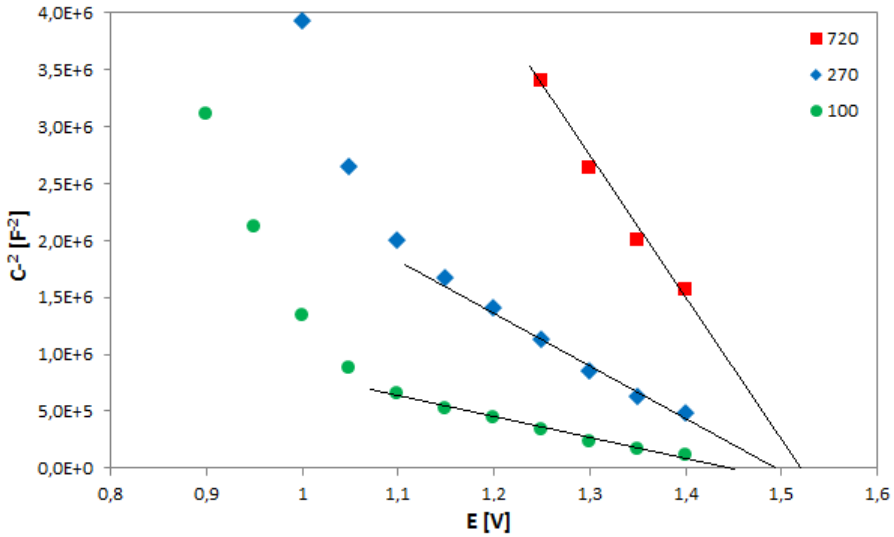

Figure 44: MS plot for x = 0.5 and frequencies 100, 270 and 720 Hz. The curves seems to have two possible linear approximations.

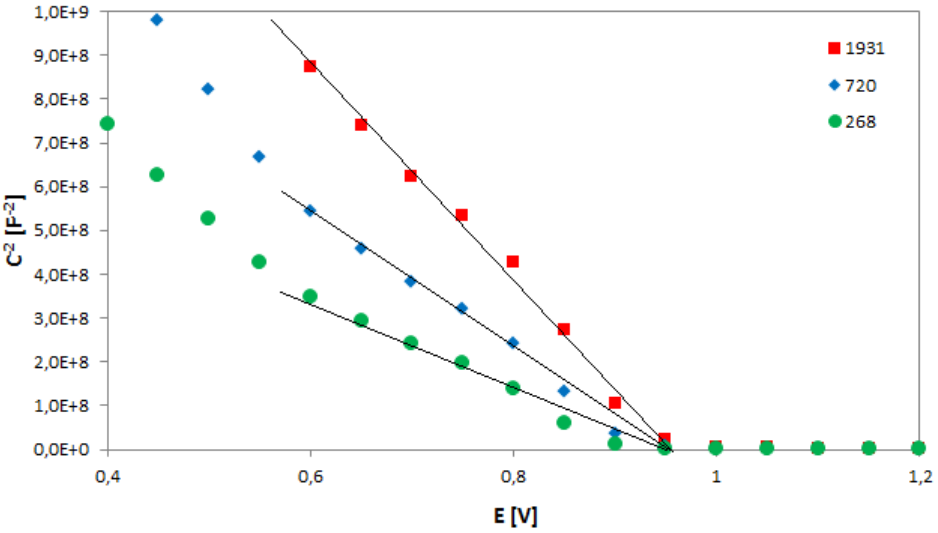

Figure 45: MS plot for x = 1 assuming the low potential V_{fb} and frequencies 268, 720 and 1931 Hz. The curves seems to have two possible linear approximations.

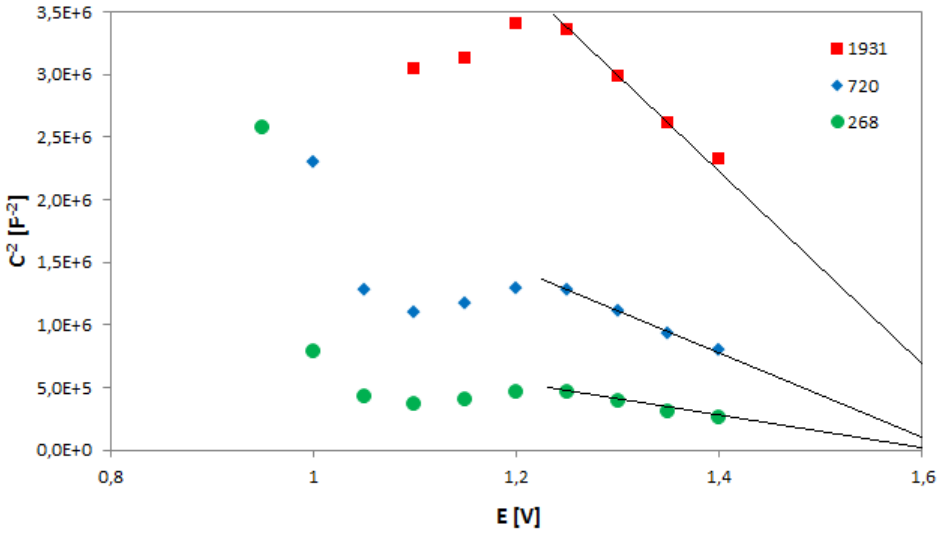

Figure 46: MS plot for x = 1 assuming the high potential V_{fb} and frequencies 268, 720 and 1931 Hz. The curves seems to have two possible linear approximations.

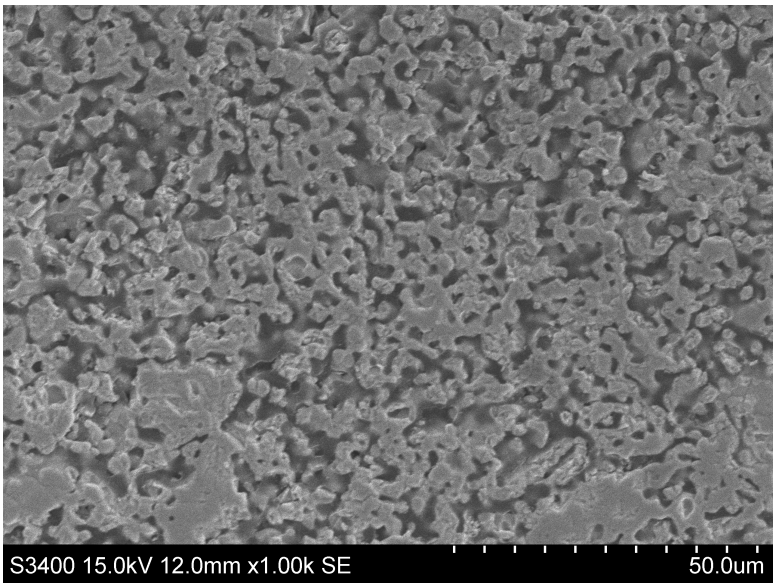

Figure 47: SEM image of x = 0 and magnification = 1k.

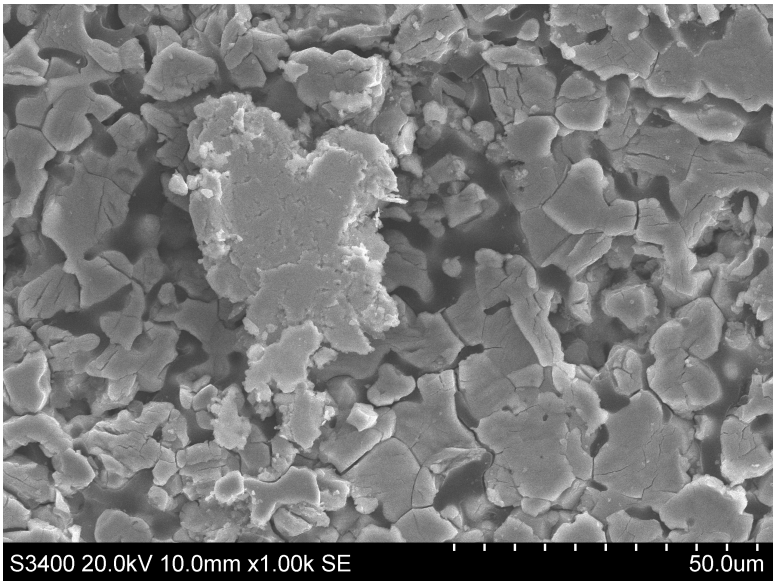

Figure 48: SEM image of x = 75 and magnification = 1k.